Planck early results

Planck early results. XXII. The submillimetre properties of a sample of Galactic cold clumps[⋆,⋆⋆]

Planck Collaboration: P. A. R. Ade[72], N. Aghanim[47], M. Arnaud[59], M. Ashdown[57,4], J. Aumont[47], C. Baccigalupi[70], A. Balbi[28], A. J. Banday[76,7,64], R. B. Barreiro[54], J. G. Bartlett[3,55], E. Battaner[78], K. Benabed[48], A. Benoît[46], J.-P. Bernard[76,7], M. Bersanelli[25,41], R. Bhatia[5], J. J. Bock[55,8], A. Bonaldi[37], J. R. Bond[6], J. Borrill[63,73], F. R. Bouchet[48], F. Boulanger[47], M. Bucher[3], C. Burigana[40], P. Cabella[28], C. M. Cantalupo[63], J.-F. Cardoso[60,3,48], A. Catalano[3,58], L. Cayón[18], A. Challinor[50,57,9], A. Chamballu[44], L.-Y Chiang[49], P. R. Christensen[67,29], D. L. Clements[44], S. Colombi[48], F. Couchot[62], A. Coulais[58], B. P. Crill[55,68], F. Cuttaia[40], L. Danese[70], R. D. Davies[56], P. de Bernardis[24], G. de Gasperis[28], A. de Rosa[40], G. de Zotti[37,70], J. Delabrouille[3], J.-M. Delouis[48], F.-X. Désert[43], C. Dickinson[56], Y. Doi[14], S. Donzelli[41,52], O. Doré[55,8], U. Dörl[64], M. Douspis[47], X. Dupac[33], G. Efstathiou[50], T. A. Enßlin[64], E. Falgarone[58], F. Finelli[40], O. Forni[76,7], M. Frailis[39], E. Franceschi[40], S. Galeotta[39], K. Ganga[3,45], M. Giard[76,7], G. Giardino[34], Y. Giraud-Héraud[3], J. González-Nuevo[70], K. M. Górski[55,80], S. Gratton[57,50], A. Gregorio[26], A. Gruppuso[40], F. K. Hansen[52], D. Harrison[50,57], G. Helou[8], S. Henrot-Versillé[62], D. Herranz[54], S. R. Hildebrandt[8,61,53], E. Hivon[48], M. Hobson[4], W. A. Holmes[55], W. Hovest[64], R. J. Hoyland[53], K. M. Huffenberger[79], N. Ikeda[51], A. H. Jaffe[44], W. C. Jones[17], M. Juvela[16], E. Keihänen[16], R. Keskitalo[55,16], T. S. Kisner[63], Y. Kitamura[51], R. Kneissl[32,5], L. Knox[20], H. Kurki-Suonio[16,35], G. Lagache[47], J.-M. Lamarre[58], A. Lasenby[4,57], R. J. Laureijs[34], C. R. Lawrence[55], S. Leach[70], R. Leonardi[33,34,21], C. Leroy[47,76,7], M. Linden-Vørnle[11], M. López-Caniego[54], P. M. Lubin[21], J. F. Macías-Pérez[61], C. J. MacTavish[57], B. Maffei[56], J. Malinen[16], N. Mandolesi[40], R. Mann[71], M. Maris[39], D. J. Marshall[76,7], P. Martin[6], E. Martínez-González[54], S. Masi[24], S. Matarrese[23], F. Matthai[64], P. Mazzotta[28], P. McGehee[45], A. Melchiorri[24], L. Mendes[33], A. Mennella[25,39], C. Meny[76,7], S. Mitra[55], M.-A. Miville-Deschênes[47,6], A. Moneti[48], L. Montier[76,7], G. Morgante[40], D. Mortlock[44], D. Munshi[72,50], A. Murphy[66], P. Naselsky[67,29], F. Nati[24], P. Natoli[27,2,40], C. B. Netterfield[13], H. U. Nørgaard-Nielsen[11], F. Noviello[47], D. Novikov[44], I. Novikov[67], S. Osborne[75], L. Pagani[58], F. Pajot[47], R. Paladini[74,8], F. Pasian[39], G. Patanchon[3], V.-M. Pelkonen[45], O. Perdereau[62], L. Perotto[61], F. Perrotta[70], F. Piacentini[24], M. Piat[3], S. Plaszczynski[62], E. Pointecouteau[76,7], G. Polenta[2,38], N. Ponthieu[47], T. Poutanen[35,16,1], G. Prézeau[8,55], S. Prunet[48], J.-L. Puget[47], W. T. Reach[77], R. Rebolo[53,30], M. Reinecke[64], C. Renault[61], S. Ricciardi[40], T. Riller[64], I. Ristorcelli[76,7], G. Rocha[55,8], C. Rosset[3], M. Rowan-Robinson[44], J. A. Rubiño-Martín[53,30], B. Rusholme[45], M. Sandri[40], D. Santos[61], G. Savini[69], D. Scott[15], M. D. Seiffert[55,8], G. F. Smoot[19,63,3], J.-L. Starck[59,10], F. Stivoli[42], V. Stolyarov[4], R. Sudiwala[72], J.-F. Sygnet[48], J. A. Tauber[34], L. Terenzi[40], L. Toffolatti[12], M. Tomasi[25,41], J.-P. Torre[47], V. Toth[31], M. Tristram[62], J. Tuovinen[65], G. Umana[36], V. Toth[31], P. Vielva[54], F. Villa[40], N. Vittorio[28], L. A. Wade[55], B. D. Wandelt[48,22], N. Ysard[16], D. Yvon[10], A. Zacchei[39], and A. Zonca[21]

(Affiliations can be found after the references)

ABSTRACT

We perform a detailed investigation of sources from the Cold Cores Catalogue of *Planck* Objects (C3PO). Our goal is to probe the reliability of the detections, validate the separation between warm and cold dust emission components, provide the first glimpse at the nature, internal morphology and physical characteristics of the *Planck*-detected sources. We focus on a sub-sample of ten sources from the C3PO list, selected to sample different environments, from high latitude cirrus to nearby (150 pc) and remote (2 kpc) molecular complexes. We present *Planck* surface brightness maps and derive the dust temperature, emissivity spectral index, and column densities of the fields. With the help of higher resolution *Herschel* and AKARI continuum observations and molecular line data, we investigate the morphology of the sources and the properties of the substructures at scales below the *Planck* beam size. The cold clumps detected by *Planck* are found to be located on large-scale filamentary (or cometary) structures that extend up to 20 pc in the remote sources. The thickness of these filaments ranges between 0.3 and 3 pc, for column densities $N_{H_2} \sim 0.1$ to 1.6×10^{22} cm^{-2}, and with linear mass density covering a broad range, between 15 and 400 $M_\odot$ pc^{-1}. The dust temperatures are low (between 10 and 15 K) and the *Planck* cold clumps correspond to local minima of the line-of-sight averaged dust temperature in these fields. These low temperatures are confirmed when AKARI and *Herschel* data are added to the spectral energy distributions. *Herschel* data reveal a wealth of substructure within the *Planck* cold clumps. In all cases (except two sources harbouring young stellar objects), the substructures are found to be colder, with temperatures as low as 7 K. Molecular line observations provide gas column densities which are consistent with those inferred from the dust. The linewidths are all supra-thermal, providing large virial linear mass densities in the range 10 to 300 $M_\odot$ pc^{-1}, comparable within factors of a few, to the gas linear mass densities. The analysis of this small set of cold clumps already probes a broad variety of structures in the C3PO sample, probably associated with different evolutionary stages, from cold and starless clumps, to young protostellar objects still embedded in their cold surrounding cloud. Because of the all-sky coverage and its sensitivity, *Planck* is able to detect and locate the coldest spots in massive elongated structures that may be the long-searched for progenitors of stellar clusters.

Key words. ISM: clouds – dust, extinction – stars: formation – ISM: structure – submillimeter: ISM – stars: protostars

---

1. Introduction

The main difficulty in understanding star formation lies in the vast range of scales involved in the process, including not only the gravitationally unstable densest and coldest structures, but also their large-scale environment. The characteristics of star formation, described by the stellar mass distribution, the formation efficiency, the evolutionary timescales, and by the modes of formation (clustered or isolated, spontaneous or triggered) are linked to the properties of the cold cores and those of their Galactic surroundings. Theory predicts that the initial mass function (IMF) is largely determined during the pre-stellar core fragmentation phase, but the latter depends on the properties of the pre-stellar cores, particularly the nature of their support against self-gravity, and their density and temperature distributions. Understanding star formation therefore also requires an understanding of the formation and evolution of dense cores. Turbulence, magnetic fields, and gravity all contribute at sub-parsec scales as well as Galactic scales (see reviews of Bergin & Tafalla 2007; McKee & Ostriker 2007; Ward-Thompson et al. 2007; Crutcher et al. 2009).

So far, ground-based (e.g., Motte et al. 1998; Johnstone et al. 2000) and *Herschel* (e.g., André et al. 2010; di Francesco et al. 2010; Könyves et al. 2010) observations of nearby star-forming regions have revealed a core mass spectrum with a slope similar to that of the IMF. This intriguing result calls for broader investigations, in particular towards the inner Galaxy, where the Galactic environment differs from that of the Solar neighbourhood, and the star formation efficiency is anticipated to be different.

The physical properties of cold cores are still poorly known, possibly because of the short duration of this phase, but mainly because of observational difficulties. The thermal emission of cold dust, intrinsically weak and blended with that of warmer components, must be sought for in the submillimetre range. A combination of continuum and molecular line studies is also needed to develop a global view of the clouds, from large scales (tens of parsecs) down to the scale of dense cores. During the past decade, the development of sensitive continuum and heterodyne detectors at millimetre and submillimetre wavelengths has significantly increased our knowledge of the properties of the cold dark clouds (see Sect. 1 in Planck Collaboration 2011s, hereafter Paper I). The *Planck*[1] and *Herschel* satellites now provide a unique opportunity for studying Galactic dust emission and in particular its dense and cold component. The first *Herschel* surveys have already provided new insights into cold cores, although limited to specific fields (André et al. 2010; Bontemps et al. 2010; Könyves et al. 2010; Men'shchikov et al. 2010; Molinari et al. 2010; Motte et al. 2010; Peretto et al. 2010; Schneider et al. 2010; Stutz et al. 2010; Ward-Thompson et al. 2010; Zavagno et al. 2010).

The *Planck* satellite (Tauber et al. 2010; Planck Collaboration 2011a) provides complementary to *Herschel* by carrying out an all-sky survey that is well suited for the systematic detection of cold cores. In Paper I, we present the first statistical results of the cores from this survey. Combining *Planck* and IRAS 100 μm data, we have built a preliminary catalogue of 10,783 cold cores (the Cold Core Catalogue of *Planck*

Objects, C3PO). A sub-sample of the most reliable detections is delivered as part of the *Planck* Early Release Compact Source Catalogue (ERCSC, see Planck Collaboration 2011c), i.e. the Early Cold Cores (ECC) catalogue. The cores from C3PO cover a wide range in properties, with: temperature, from 7 K to 19 K, with a peak around 13 K; density from 10^2 cm^{-3} to 10^5 cm^{-3}, with an average value of 2×10^3 cm^{-3}; mass from 0.4 to 2.4×10^5 $M_\odot$; and size ranging from 0.2 to 18 pc. The sources are found to be extended, and more importantly are elongated, with a distribution of aspect ratios extending up to 4 and peaking at twice the beam size of the *Planck*-HFI instrument. As discussed in Paper I, these properties better match the definition of "clumps" rather than "cores" (see Williams et al. 2000; Bergin & Tafalla 2007). Clumps may contain dense cores, which are likely the precursors of individual or multiple stars. Thus, the main population seen with *Planck* does not correspond to single pre-stellar cores, but ensembles of cold substructures. A detailed study of the *Planck* cold objects requires observations at higher resolution. This is the main objective of the *Herschel* open time key program "Galactic Cold Cores" that is dedicated to following up of a sample of *Planck* cores.

In this paper we present the first detailed analysis of ten representative sources from the C3PO catalogue. The targets have been selected to cover different types of clump, spanning a wide range of mass, temperature, and density, and located in different environments, ranging from high latitude cirrus to nearby and distant molecular complexes. We combine the *Planck* data with available ancillary data (in particular IRIS, 2MASS and AKARI) and dedicated follow-up observations with *Herschel* and ground-based radio telescopes. Using these ancillary data, we seek to confirm the *Planck* detections and to demonstrate the reliability of the method which used only *Planck* and IRAS data to determine the source parameters that enter the C3PO catalogue (Paper I) and ECC catalogue (Planck Collaboration 2011c,v). The higher resolution continuum and line data make it possible to examine the internal structure of the *Planck* sources. They provide the first hints about the process of internal fragmentation and the physical state of the compact cores at scales below the size of the *Planck* beam. These properties are essential for the interpretation of the full C3PO catalogue and will be a major topic for the projects carrying out follow-up studies of C3PO and ECC catalogue sources.

After describing the observational data set and the source sample selection (Sect. 2), we explain the analysis methods used to derive physical properties for the cores (Sect. 3). The main results are presented in Sect. 4. By fitting spectral energy distributions (SEDs) we derive temperatures, emissivity spectral indices, and column densities for the cores and the surrounding fields, and estimate the linear mass densities, masses and bolometric luminosities of the cores (Sect. 4.1). The small-scale structures within the *Planck* clumps are studied with the help of *Herschel* and AKARI data (Sect. 4.3.1), and the gas properties of a few cores are derived from molecular line data (Sect. 4.3.3). Following a discussion of the physical characteristics of the *Planck* cores, we present our summary and perspectives for the future in Sect. 6.

2. Observations

2.1. The sources

We have selected from the C3PO ten sources with high reliability, signal-to-noise ratio $S/N \geq 8$, and low colour temperature, $T \leq 14$ K (see Paper I). An initial Monte Carlo sampling of

---

the full C3PO catalogue was performed to prepare a candidate list that covered the full range in Galactic position, temperature, flux, and column density. Further selection was made by examining the *Planck* data and ancillary information from IRIS (Miville-Deschênes & Lagache 2005), 2MASS extinction (Skrutskie et al. 2006), and CO line data from Dame et al. (2001) and NANTEN surveys (e.g., Fukui et al. 1999), as well as IRAS and AKARI point source catalogues and by cross-checking the sources with the SIMBAD database. The selected sources represent different large-scale morphologies and environments, including filaments, isolated and clustered structures and high-latitude cirrus clouds. One key criterion was the knowledge of the source distance, derived either with an extinction method (Marshall et al. 2006), by association with a known molecular cloud complex, or through a kinematic distance estimate (see Paper I). Nine out of the ten sources have already been observed with *Herschel* as part of the open time key program "Galactic cold cores." In particular, the sample includes the three targets observed during the *Herschel* science demonstration phase (SDP, see Juvela et al. 2010, 2011). Half of the sources in the sample are in the *Planck* ECC. This is mainly due to the criteria used to select the most reliable detections from the C3PO full catalogue (see Paper I): with $T < 14$ K for the colour temperature corresponding to the aperture photometry SED, and a high signal to noise ratio for the source detection ($S/N > 15$).

The targets are listed in Table 1 and presented in detail in the Appendix. The ten sources that we focus on will hereafter be referred to by the labels S1 through S10.

2.2. Planck data

Planck (Tauber et al. 2010; Planck Collaboration 2011a) is the third generation space mission to measure the anisotropy of the cosmic microwave background (CMB). It observes the sky in nine frequency bands covering 30–857 GHz with high sensitivity and angular resolution from 31′ to 5′. The Low Frequency Instrument (LFI; Mandolesi et al. 2010; Bersanelli et al. 2010; Mennella et al. 2011) covers the 30, 44, and 70 GHz bands with amplifiers cooled to 20 K. The High Frequency Instrument (HFI; Lamarre et al. 2010; Planck HFI Core Team 2011a) covers the 100, 143, 217, 353, 545, and 857 GHz bands with bolometers cooled to 0.1 K. Polarisation is measured in all but the highest two bands (Leahy et al. 2010; Rosset et al. 2010). A combination of radiative cooling and three mechanical coolers produces the temperatures needed for the detectors and optics (Planck Collaboration 2011b). Two data processing centres (DPCs) check and calibrate the data and make maps of the sky (Planck HFI Core Team 2011b; Zacchei et al. 2011). *Planck*'s sensitivity, angular resolution, and frequency coverage make it a powerful instrument for Galactic and extragalactic astrophysics as well as cosmology. Early astrophysics results are given in Planck Collaboration, 2011h–w.

We use data from the *Planck*-HFI bands at 857 GHz, 545 GHz and 353 GHz that cover the main peak of the cold dust emission. By restricting ourselves to these highest frequencies, we can perform the analysis at the best angular resolution provided by *Planck*, i.e., ~4.5′ full width at half-maximum (FWHM).

Figure 1 displays the 857 GHz surface brightness maps for each 1°×1° field. The cores are located at the centres of the maps and show dust emission that ranges from 10 to 220 MJy sr^{-1}. They are embedded in extended structures whose shape varies from large filaments (S4, S5, S6, S7 and S10) to more isolated and apparently compact morphologies. Most cores are extended

and elongated compared to the *Planck* beam. As discussed in Paper I, the ellipticity and extension of the cores are not biased by the local beam shape. As an illustration, Fig. A.5 shows the comparison between the local Point Spread Function provided by the FEBeCoP tool (Mitra et al. 2011) with the elliptical Gaussian fit of the sub-sample detections. Typical sizes are from 0.2 to 11 pc. Some cores (S2, S8, and S9) are located near bright, warmer regions, where the intensities are higher by up to a factor of 10. In a few cases, the environment exhibits sharp edges, at large scale (see in particular S1, S3 and S7).

The full set of HFI maps (1°×1° fields from 857 to 100 GHz) for each source are shown in Figs. A.1–A.3. These maps have been derived from the HEALPix sky maps (Górski et al. 2005). With the exception of source S2, the cold source at the centre of the maps is usually visible down to 143 GHz. At 100 GHz the sources become difficult to detect because of the falling intensity of the dust spectrum. Only the Musca filament is clearly visible even at 100 GHz, although the surface brightness of the source is low (~0.15 MJy sr^{-1}).

Comparison with the 100 μm maps from IRIS (Miville-Deschênes & Lagache 2005) confirms the conclusion of previous submillimetre surveys (using PRONAOS, Archeops, BLAST, and ground-based telescopes) that the cold dust emission is not traced by the 100 μm data, but must be studied using longer wavelengths. The IRIS maps are dominated by the warmer and more extended structure around the cores. This is the basis of the source detection method CoCoCoDeT (Cold Core Colour Detection Tool), that was described in detail in Montier et al. (2010) and in Paper I (Sect. 2.4). It uses as a template the spectrum of the warm emission component estimated from the IRIS 100 μm map. Subtraction of the warm component results in residual maps of the cold emission component from which source fluxes are derived. The detection process is applied independently to the 857, 545, and 353 GHz maps, after smoothing HFI and IRIS data to the same angular resolution of 4.5′. The main steps of the method and the core extraction process are illustrated in the Appendix (in Fig. A.4) for S1. The residual 100 μm signal that remains when a background model is subtracted from the IRIS map (see Paper I) is still needed to constrain the temperature of the cold core SEDs, which typically peak in the range 200–300 μm. The analysis of Sect. 4 will also test the accuracy of this procedure. The coordinates, distances, fluxes densities, and sizes of the selected *Planck* cores are given in Table 1. The values listed there are taken directly from the C3PO catalogue (see Paper I and Sect. 3.1).

2.3. Herschel observations

The *Herschel* photometric observations were carried out with the PACS and SPIRE instruments (Pilbratt et al. 2010; Poglitsch et al. 2010; Griffin et al. 2010). Three fields, S8, S9, S10 (corresponding to the source names PCC249, PCC288, and PCC550) were observed in November and December 2009 as part of the *Herschel* SDP. The other fields were observed between July and September 2010. Most observations were performed separately with PACS (100 and 160 μm) and with SPIRE (250, 350 and 500 μm) in scan mapping mode. Because of the larger field size, S5 and S9 were observed in parallel mode using both instruments simultaneously. The observations employed two orthogonal scanning directions, except for the PACS observations of PCC288 where three scanning directions were used. The data were reduced with *Herschel* interactive processing environment (HIPE), using the official pipeline with the addition of
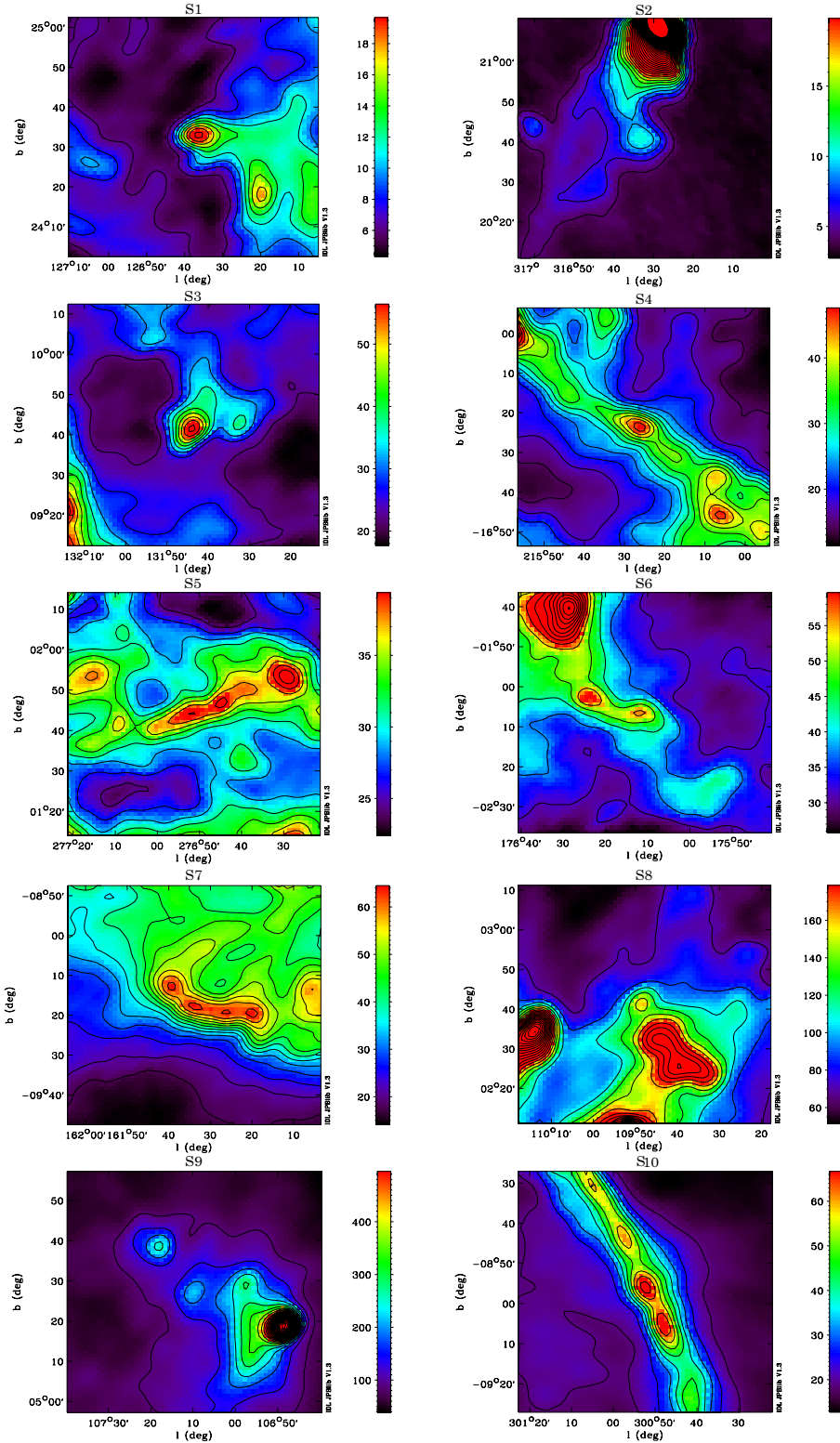
Fig. 1. *Planck*-HFI brightness emission maps at 857 GHz. The colour scale is in MJy sr^{-1}. Note the large dynamic range of the *Planck* cold clumps from 10 MJy sr^{-1} (S2) to 250 MJy sr^{-1} (S9).

specialised reduction routines to take advantage of the orthogonal scans for deglitching PACS data and to remove SPIRE scan baselines. The PACS maps were created using the MADmap algorithm (Cantalupo et al. 2010). The SPIRE maps are the product of direct projection onto the sky and averaging of the time ordered data, with a baseline correction.

As for most bolometer observations without an absolute calibrator, the zero level (or offset) of the PACS and SPIRE data are arbitrary. We therefore compared the *Herschel* and PACS

data with the predictions of a model constrained by the *Planck* and IRAS data. The model uses the all-sky dust temperature maps described in Planck Collaboration (2011o) to infer the average radiation field intensity for each pixel at the common resolution level for the *Planck* and IRAS data. The DUSTEM model (Compiègne et al. 2010) with the above value for the radiation field intensity was used to predict the expected brightness in the *Herschel*-SPIRE and PACS bands, using the nearest available *Planck* or IRAS band for normalisation and taking into

Table 1. Source selection.

Source name		l (deg)	b (deg)	S/N	S_{857} (Jy)	S_{545} (Jy)	S_{353} (Jy)	$\theta_{\mathrm{Min}}{}^a$ (arcmin)	$\theta_{\mathrm{Maj}}{}^a$ (arcmin)	$\langle\theta\rangle^a$ (arcmin)	d (pc)	Complex
Planck−G126.6+24.5	**S1**	126.62	24.55	44.0	62.0	22.5	5.2	4.9	7.6	6.1	150	Polaris flare
Planck−G20.7+20.0	**S2**	316.53	20.68	20.0	35.6	12.7	2.9	7.2	9.1	8.1	550	Cometary Globule
Planck−G131.7+9.7	**S3**	131.74	9.70	38.2	185.8	77.5	19.7	6.3	8.0	7.1	200	Cepheus flare
Planck−G215.2−16.4	**S4**	215.44	−16.38	24.0	85.9	34.9	9.2	5.0	7.4	6.1	450	Orion
Planck−G276.9+1.7	**S5**	276.87	1.73	8.5	88.4	34.4	9.5	4.6	18.8	9.3	2000	Vela
Planck−G176.2−2.1	**S6**	176.18	−2.11	25.8	116.8	51.0	13.2	5.0	11.5	7.6	2000	Perseus Arm
Planck−G161.6−9.2	**S7**	161.56	−9.29	15.0	196.5	78.1	20.9	5.5	14.9	9.1	350	PerOB2
Planck−G109.8+2.7	**S8**	109.79	2.71	16.1	272.4	122.8	33.3	5.1	9.3	6.9	800	Cephee
Planck−G107.2+5.5	**S9**	107.17	5.45	23.6	490.2	185.5	49.5	4.4	8.3	6.1	800	Cep−OB3b
Planck−G300.9−9.0	**S10**	300.86	−8.96	82.7	267.3	98.8	24.3	4.2	15.2	8.0	225	Musca

Notes. $^{(a)}$ The values are not beam deconvolved; the corresponding ellipse contours are shown in Figs. 3–5.

account the appropriate colour correction in the *Herschel* filters. The predicted brightness was correlated with the observed maps smoothed to the *Planck* and IRAS resolution over the region observed with *Herschel* and the gain and offsets were derived from this correlation. We have used these gain and offset inter-calibration values in order to convert the maps from Jy beam^{-1} and Jy pix^{-1} (SPIRE and PACS, respectively) into brightness units (MJy sr^{-1}).

2.4. AKARI observations

The AKARI satellite (Murakami et al. 2007) has conducted all-sky surveys at infrared wavelengths centred at $9\,\mu$m, $18\,\mu$m, $65\,\mu$m, $90\,\mu$m, $140\,\mu$m, and $160\,\mu$m. We use the observations made by the FIS instrument in the wide far-infrared bands of $90\,\mu$m and $140\,\mu$m. The accuracy of the calibration is currently estimated to be 26% at $90\,\mu$m and 33% at $140\,\mu$m, and the beam sizes of these two bands are $\sim$39″ and 58″, respectively. For details of the AKARI far-infrared all sky survey, see Doi et al. (2009).

2.5. Molecular line data

We have carried out "fast" observations of different CO isotopic lines in some 60 *Planck* cold core candidate fields for the *Herschel* follow-up programme, five of which are included in the present sample.

The Onsala 20-m telescope was used for ^{12}CO $J = 1 \rightarrow 0$, ^{13}CO $J = 1 \rightarrow 0$, and C^{18}CO $J = 1 \rightarrow 0$ observations in December 2009 and April 2010. An area of a few arcmin in diameter was mapped around the position of the *Planck* source S3 and the sources in the SDP fields S8 and S9. The observations were carried out in frequency switching mode, with frequency throws of $\pm$10 MHz. The Onsala beam size is approximately $\sim$33″ and the typical rms noise in the ^{13}CO and C^{18}O spectra was below 0.1 K per a channel of 0.07 km s^{-1}.

The APEX observations of field S10 were made in July 2010. The size of the ^{13}CO $J = 2 \rightarrow 1$ map is $\sim$5′ and the typical rms noise is below 0.2 K. The observations were made in position switching mode, using a fixed off position of $\alpha = 12^{\mathrm{h}}18^{\mathrm{m}}58.19^{\mathrm{s}}$ and $\delta = -71^{\mathrm{d}}42'30.81''$ (*J*2000). The APEX beam size at 220 GHz is $\sim$28″.

The IRAM-30m observations were performed in July and October 2010. The EMIR receivers E090 (3 mm) and E230 (1 mm) were used in parallel with the high resolution correlator

(VESPA). The most important parameters for the different settings are given in the Appendix in Table A.1. Maps of 3′×3′ were performed using on-the-fly (OTF) mode combined with frequency switching. A summary of the observations and the main results obtained are presented in Sect. 4.3.3.

3. Methods

3.1. Photometry and SEDs

3.1.1. *Planck* and IRAS photometry

The method for estimating the photometry for the C3PO catalogue has been described in detail in Montier et al. (2010) and Paper I (Sect. 2.4). We recall here only the main steps of the detection and flux extraction process:

1. for each pixel, and for each frequency, the warm background colour (C_{bkg}) is estimated as the median value of the ratio of the *Planck* to $100\,\mu$m emission maps (I_ν/I_{100}) within a 15′ radius disc;
2. for each *Planck* frequency, the contribution of the warm component is obtained by extrapolation from $100\,\mu$m through $I_\nu^{\mathrm{w}} = C_{\mathrm{bkg}} \times I_{100}$;
3. the cold residual map is computed by subtracting the warm component from the *Planck* map;
4. the cold source detection is performed using a thresholding method applied on the cold residual map, with the criterion $S/N > 4$;
5. the source shape is estimated by fitting a 2D elliptical Gaussian to the colour map I_{857}/I_{100};
6. the flux density at $100\,\mu$m is derived by fitting an elliptical Gaussian plus a polynomial surface for the background;
7. the warm template at $100\,\mu$m is corrected by removing the source contribution that was estimated in the previous step;
8. aperture photometry at 857, 545, and 353 GHz is performed on the cold residual maps, with the aperture determined by the source shape from step 5.

The photometric uncertainties associated with this method have been estimated with a Monte Carlo analysis (see Paper I, Sect. 2.5); they are 40% for IRAS $100\,\mu$m and 8% in the *Planck* bands. The additional calibration uncertainties to be taken into account are 13.5% and 7%, respectively, for IRIS (Miville-Deschênes & Lagache 2005) and the HFI bands 857, 545, and 353 GHz (Planck HFI Core Team 2011b). As described

in Paper I, the elliptical Gaussian fit performed in step 5 leads to an estimate of the minor and major axis lengths (σ_{Min} and σ_{Maj}, respectively), related to the FWHM values, i.e., θ_{Min} and θ_{Maj} of a Gaussian by $\sigma = \theta/\sqrt{8\ln(2)}$. This method does not include any beam deconvolution. The fluxes and FWHM values are given for each source in Table 1, and the corresponding elliptical fit contours (traced with θ_{Min} and θ_{Maj} as minor and major axis lengths) are shown in Figs. 3–5.

The 353 GHz band includes some contribution from the CO $J = 3 \rightarrow 2$ molecular line. The magnitude of this effect has been estimated in Planck HFI Core Team (2011b) using data from ^{12}CO $J = 1 \rightarrow 0$ surveys, together with an estimated average line ratio of $J = 3 \rightarrow 2$ to $J = 1 \rightarrow 0$, and knowledge of the 353 GHz band spectral response. The derived correction factor is 171 μK in thermodynamic temperature for a CO $J = 1 \rightarrow 0$ line area of 1 K km s^{-1}. The correction should be small, but the exact effect is hard to estimate for our sources because of the lack of high spatial resolution CO data and because the CO excitation towards cold cores may differ significantly from the average values assumed in deriving the above factor. We therefore present results without making a correction for the CO contribution, but comment on its possible influence later.

3.1.2. Photometry with ancillary data

When using *Herschel* and AKARI data, the fluxes are estimated at a different resolution and with direct aperture photometry. The maps are convolved to a resolution of 37″ (for *Herschel* and AKARI 90 μm), 58″ (for *Herschel* and AKARI 90 μm and 140 μm), or 4.5′ (when including *Planck* and IRIS data). In each case the aperture has a radius equal to the FWHM of the smoothed data and the background is subtracted using the 30% quantile value within a reference annulus that extends from 1.3× FWHM to 1.8× FWHM. In order not to be affected by possible emission from transiently heated grains, the fits employ only data at wavelengths longer than 100 μm. The statistical uncertainty of the flux values is derived from the surface brightness fluctuations in the reference annulus. As above, the calibration uncertainty is taken to be 7% for the *Planck* channels and 13.5% for IRIS 100 μm. For *Herschel* we assume a 15% calibration uncertainty for PACS and 12% for SPIRE.

3.2. Estimation of temperatures, spectral indices, and optical depths

Since the dust thermal emission is optically thin in the submillimetre range, the source SEDs can be modelled as a modified blackbody of the form

$$S_\nu = \tau_\nu B_\nu(T_c)\,\Omega_{\text{cl}} \tag{1}$$

where S_ν is the flux density integrated over the clump solid angle Ω_{cl} (common to all frequencies), $\tau_\nu = N_{\text{H}_2}\mu m_{\text{H}}\kappa_{\nu_0}(\nu/\nu_0)^\beta$ is the dust optical depth, and B_ν is the Planck function at the dust colour temperature, T_c. Here N_{H_2} is the H$_2$ gas column density, $\mu = 2.33$ the mean mass per particle, m_{H} the mass of the proton, κ_{ν_0} the mass absorption coefficient at frequency ν_0 and β the dust emissivity spectral index. The SED may be rewritten as

$$S_\nu = A B_\nu(T_c)\,\nu^\beta \tag{2}$$

to separate the three quantities (assumed independent) which can be derived from the fit: amplitude $A \propto N_{\text{H}_2}\kappa_{\nu_0}$; spectral index β; and effective temperature T_c. The χ^2 minimisation search operates in the (A, T_c, β) space and takes into account the colour

corrections for the *Planck* bands described in Planck HFI Core Team (2011a). In the fitting procedure, we consider only the flux error bars associated with the photometry method, i.e., 40% for IRIS and 8% for HFI bands. In a second step, we compute the final error bars on T_c and β by adding the contribution from calibration uncertainties; these have to be considered separately because the HFI calibration errors are not independent of eachother. In Paper I the size of this effect was estimated using a grid of T_c and β values, and was found to be small ($\leq 2.5\%$ for T_c and $\leq 2\%$ for β) compared to the uncertainties of the flux extraction method. The final uncertainties in T_c and β are obtained as a quadratic sum of the two contributions. They do not include the correlations between T_c and β inherent in the fitting procedure itself.

Applying the same fitting method pixel by pixel to the IRIS 100 μm and HFI 857, 545, and 353 GHz surface brightness images ($1° \times 1°$), we calculate maps of the dust colour temperature and the emissivity index. Here the flux error bars are the quadratic sum of the noise map and the calibration uncertainties. The averaged column densities of the clumps are then derived from the observed flux at $\nu_0 = 857$ GHz and the dust colour temperature inferred from the fit:

$$N_{\text{H}_2} = \frac{S_{\nu_0}}{\Omega_{\text{cl}}\mu m_{\text{H}}\kappa_{\nu_0} \times B_{\nu_0}(T_c)} \tag{3}$$

with $\Omega_{\text{cl}} = \pi\sigma_{\text{Maj}}\sigma_{\text{Min}}$.

The value of κ_ν is a main source of uncertainty. Large variations exist between dust models, depending on properties of the dust (see Beckwith et al. 1990; Henning et al. 1995): composition (with or without ice mantles); structure (compact or fluffy aggregates); and size. Both models and observations show that κ_ν increases from the diffuse medium to dense and cold regions by a factor of 3–4 (Ossenkopf & Henning 1994; Kruegel & Siebenmorgen 1994; Stepnik et al. 2003; Juvela et al. 2011; Planck Collaboration 2011u). For this study, we adopt the dust absorption coefficient of Beckwith et al. (1990) inferred for high-density environments (Preibisch et al. 1993; Henning et al. 1995; Motte et al. 1998):

$$\kappa_\nu = 0.1 \text{cm}^2\text{g}^{-1}\,(\nu/1000\,\text{GHz})^\beta, \tag{4}$$

with a fixed emissivity index of $\beta = 2$. The reference frequency $\nu_0 = 857$ GHz chosen to estimate N_{H_2} is such that the extrapolation from 1000 GHz with $\beta = 2$ (instead of the fitted spectral index) introduces an uncertainty on N_{H_2} of less than 30%. At a distance d, the mass of the clump is simply $M = N_{\text{H}_2}^{\text{cl}}\Omega_{\text{cl}}\mu m_{\text{H}}d^2$ or

$$M = \frac{S_{\nu_0}d^2}{\kappa_{\nu_0}B_{\nu_0}(T_c)}. \tag{5}$$

4. Results

4.1. Physical parameters derived from Planck and IRIS data

The cold clump SEDs determined using the *Planck* HFI and IRIS flux densities are shown in Fig. 2. As discussed in Sect. 3.1.1, these SEDs are those of the cold dust residual. The values obtained for the dust temperature and emissivity spectral index are shown in the frames of the figure. Using the method described in Sect. 3.2, we infer the gas column density, bolometric luminosity, and mass of each clump (Table 2). All these parameters (T, β, N_{H_2}) are values which are *averaged* over the
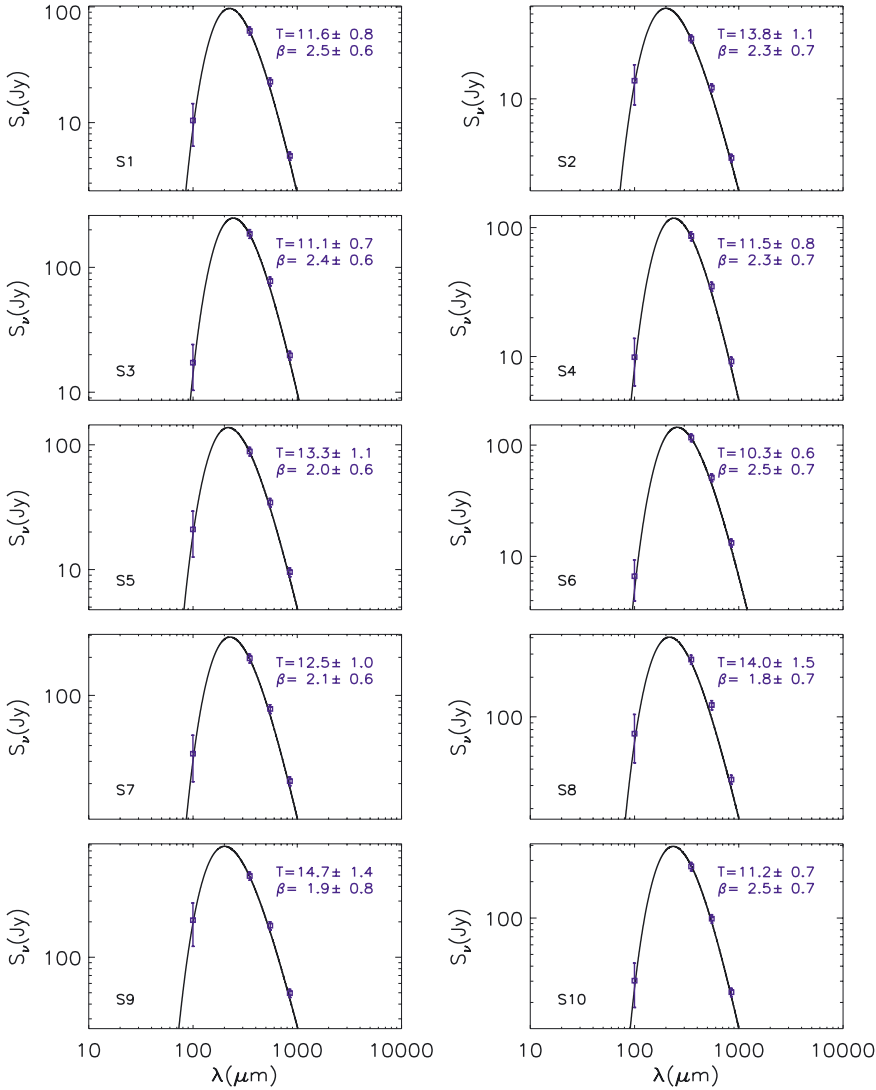
Fig. 2. SEDs and fit parameters (T, β) obtained combining *Planck* HFI and IRIS flux densities integrated over the clump in the cold residual maps.

line-of-sight and the extent of the cold clumps, which reach the parsec-scale. Denser and/or colder structure is to be expected on smaller scales. These averaged temperatures vary between 10.3 and 14.7 K, and the dust emissivity spectral indices range between 1.8 and 2.5.

The column densities are distributed around a mean of $7.5 \times 10^{21}\,\mathrm{cm}^{-2}$, with a few of the largest values being above $\sim 10^{22}\,\mathrm{cm}^{-2}$. These relatively moderate column densities also correspond to averaged values over the extent of the clumps. The clumps are likely to be heterogeneous, with denser substructures that will be studied with higher angular resolution data in Sect. 4.3.1. The masses of the sample cover a large range from 3.5 to 1800 $M_\odot$. The highest-mass object, S6, is also the coldest source of the sample, and it is quite extended ($\sim 2.9 \times 6.7$ pc); these properties make this source an interesting candidate for being a high mass star-forming precursor in its early stages. More generally, the sizes of the source sample are rather large, in the range 0.2–11 parsecs, which confirms that they should be better classified as "clumps" rather than "cores," according to the terminology used for nearby molecular clouds (e.g., Williams et al. 2000; Motte et al. 2007). Scales typically considered for "dense cores" and "clumps" are ~ 0.1 pc and ~ 1 pc, respectively.

As noted in Paper I, most of the cold clumps found with the CoCoCoDet procedure are elongated, with aspect ratios significantly larger than unity. The maps of Fig. 1 show that these

clumps are not isolated, but are, in many cases, substructures of long filaments, not always straight. Without direct estimates of the density it is difficult to assess that they are actual filaments, denser than their environment. However, their brightness contrast above the background is a few, in the case of S4, S5, S6 and S10, suggesting actual density enhancements given their small thickness. Their length, estimated from their angular size in the maps of Fig. 1 and their distance, ranges from about 5 pc for S10 to 18 pc for S5.

Because of this, we choose to focus not on the clump mass, that depends on the size of the clump derived from the detection procedure, but on the mass per unit length of the filament at the position of the cold clump. This mass per unit length (or linear mass density) is given by $m = 16.7\,M_\odot\,\mathrm{pc}^{-1}\,N_{21}\theta_{\mathrm{Min}}$, where N_{21} is the clump column density expressed in units of $10^{21}\,\mathrm{cm}^{-2}$ and θ_{Min}, the half-power thickness of the clump identified in the *Planck* maps, is taken as the width of the filament. The linear mass densities are given in Table 2 for all clumps, including those with an aspect ratio only slightly larger than unity. However, they should be considered only as an approximate guide to the linear mass density at the location of the clump.

The linear mass densities vary by a factor ~ 30 and compare well with those inferred from molecular lines. The range of values (15 to 400 $M_\odot\,\mathrm{pc}^{-1}$) is characteristic of regions of massive or intermediate-mass star formation, such as Orion and ρ Oph
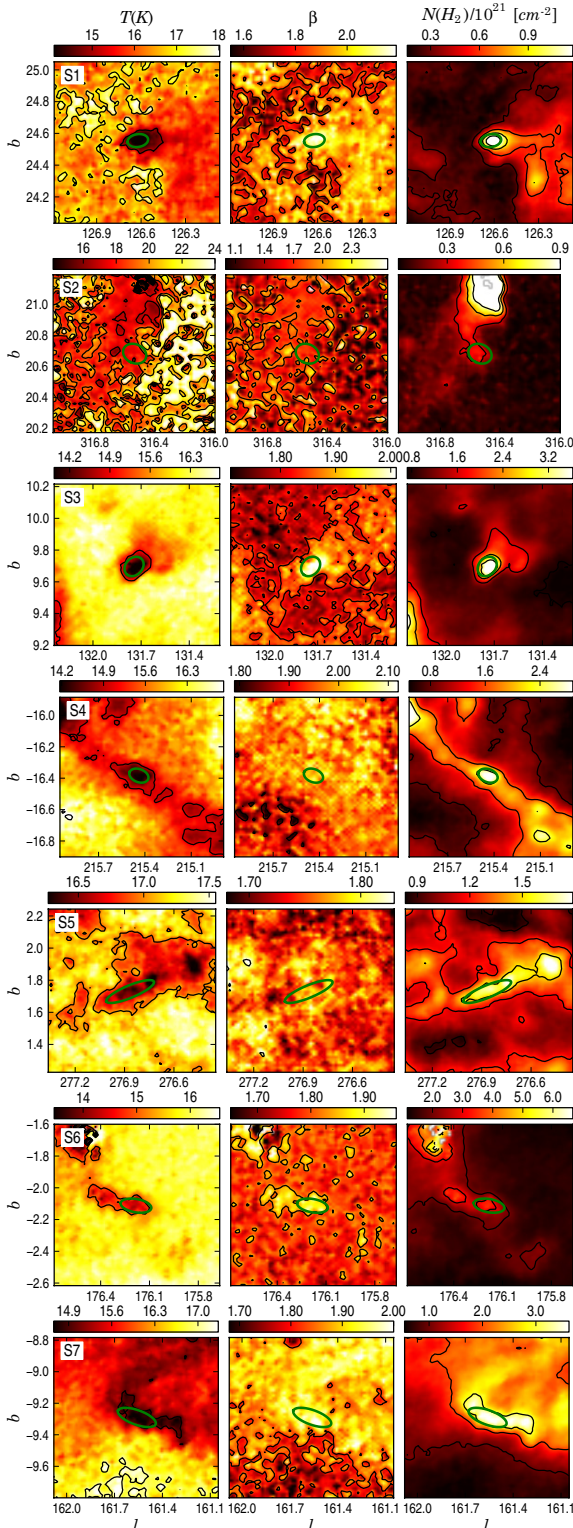
Fig. 3. Maps of dust colour temperature, emissivity spectral index and column density for each clump field (the three SDP fields are shown in Juvela et al. (2011) using *Herschel* maps). The N_{H_2} contours correspond to the ticks on the colour bar. For T and β, the contours are shown respectively at 2K intervals and for $\beta = 1.85$. The ellipses trace the FWHMs of the *Planck* clumps as inferred from the fit (see Table 1).

(Hily-Blant et al. 2004). The linear mass densities of the most tenuous filaments ($<1\ M_\odot\ pc^{-1}$, Falgarone et al. 2001) are not found in the present sub-sample of *Planck* cold clumps.

Many of the cold clumps detected by *Planck* therefore appear as cold substructures within larger scale filamentary structures that have length up to ~20 pc in the *Planck* maps and with parsec-scale thickness (S5, S6, S7). The thinnest filaments found are only a few parsec long and with thickness of a few 0.1 pc (S10).

At this stage of the analysis, it is difficult to assess the exact nature of the sources, i.e., discriminating between protostellar objects and starless clumps. We can however use the temperature and bolometric luminosity estimates as first indicators of the evolutionary stage of the sources. Such an approach was proposed by Netterfield et al. (2009) and Roy et al. (2011) in their analysis of the cold cores detected with the balloon-borne experiment, BLAST, in the Cygnus-X and Vela surveys. Among the values obtained for the ratio L/M in our sample (ranging from 0.13 to 0.91 $L_\odot/M_\odot$), it is interesting to note that the three highest (with $L/M > 0.6\ L_\odot/M_\odot$) are associated with $T > 14$ K dust sources S2, S8 and S9. As we will see in Sect. 4.3.1, the *Planck* clumps in these fields harbour warm dust sources, and two of them are associated with young stellar objects.

4.2. Colour temperature and spectral index maps

Figure 3 shows the $1° \times 1°$ maps for dust colour temperature and dust spectral index that were estimated using the IRAS 100 μm data and the three highest frequency HFI channels (see Sect. 3.2) without background removal. The three *Herschel* SDP fields (S8, S9 and S10) are not presented here, because the analysis of T and β was already described in detail in Juvela et al. (2011).

Except for the faint (and not so cold) source S2, a clear signature of cold dust emission is visible directly on these temperature maps at the location of the clumps. The colour temperature characterizing the line-of-sight integrated intensity in the direction of the clump is typically about 14 K, warmer by a few Kelvin than the clump temperature deduced from its SED after warm background subtraction. The clumps are embedded within extended structures in the temperature range 16–18 K. For reference, dust in the diffuse medium of the local Galactic neighbourhood has a temperature of around 17.5 K (Boulanger et al. 1996; Schlegel et al. 1998). In several cases (S4, S5, S6 and S7) the cold clumps appear as the coldest spot (or one of the coldest spots) along filamentary structures, which are already colder than the larger scale environment. The temperature and column density maps are correlated, with the coldest structures corresponding, as expected, to the most opaque parts of the field at the angular resolution probed by *Planck*. The sharp edges seen in the intensity maps of the fields S1, S3 and S7 are also clearly associated with column density sharp transition. This may be the signature of shock compression and triggering core formation that should be investigated in further studies.

We have compared the results on column densities with extinction measurements. Extinction is calculated with the NICER method (Lombardi & Alves 2001) using stars from the 2MASS catalogue (Skrutskie et al. 2006). The A_V maps of the fields are derived assuming an extinction curve that corresponds to $R_V = 3.1$. Preliminary extinction maps are created using nearby fields where IRAS 100 μm data indicates a low dust column density. The A_V maps obtained with this method are shown in the Appendix (in Fig. A.6) at 4.5′ resolution. A clear signature is visible, with an increase by about a factor of 2 in A_V toward the clumps. The A_V values derived (~2–5 mag) are consistent with the previous N_{H_2} estimates of several times $10^{21} cm^{-2}$, derived from the SEDs.
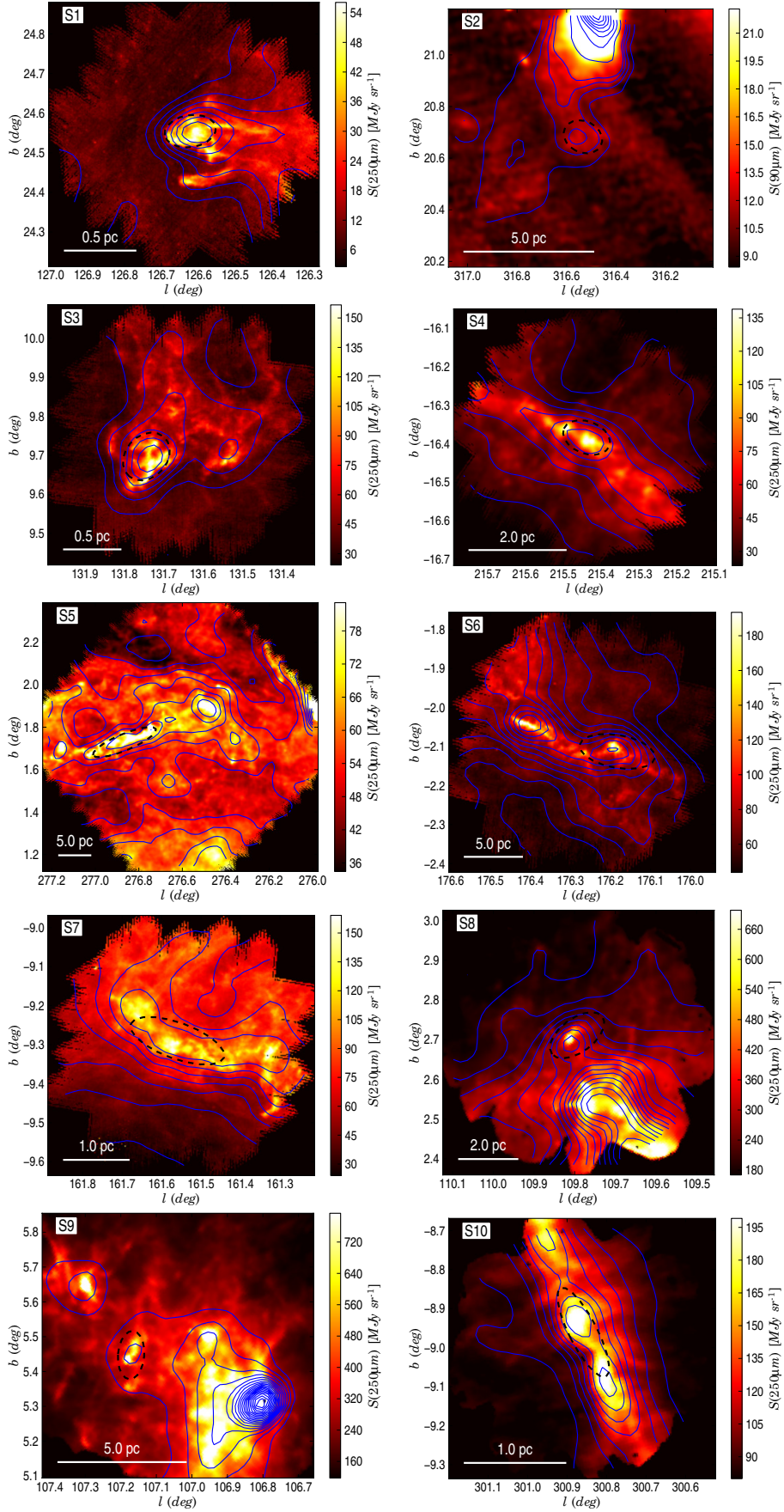
Fig. 4. *Planck* 857 GHz surface brightness contours on *Herschel* SPIRE maps at 250 μm. The source S2 has not been observed with *Herschel* and the displayed image corresponds to the AKARI 90 μm wide filter. As in Fig. 3, the dashed ellipses are tracing the estimated size of the *Planck* cold clump.

Table 2. Clump physical parameters derived from *Planck* SEDs.

Source	T_c (K)	β	$\theta_{\mathrm{Min}}{}^a$ (pc)	$\theta_{\mathrm{Maj}}{}^a$ (pc)	N_{H_2} (cm^{-2})	m^b ($M_\odot$ pc^{-1})	M ($M_\odot$)	L ($L_\odot$)	L/M ($L_\odot/M_\odot$)
S1	11.6 ± 0.8	2.5 ± 0.6	0.2	0.3	4.4×10^{21}	15	3.5	1.0	0.28
S2	13.8 ± 1.1	2.3 ± 0.7	1.2	1.5	8.0×10^{20}	16	15.0	11.0	0.72
S3	11.1 ± 0.7	2.4 ± 0.6	0.4	0.5	1.1×10^{22}	77	22.0	4.3	0.19
S4	11.5 ± 0.8	2.3 ± 0.7	0.7	1.0	6.3×10^{21}	74	44.0	11.0	0.24
S5	13.3 ± 1.1	2.0 ± 0.6	2.7	11.0	1.7×10^{21}	77	520.0	270.0	0.52
S6	10.3 ± 0.6	2.5 ± 0.7	2.9	6.7	8.4×10^{21}	400	1800.0	230.0	0.13
S7	12.5 ± 1.0	2.1 ± 0.6	0.6	1.5	4.9×10^{21}	49	45.0	17.0	0.37
S8	14.0 ± 1.5	1.8 ± 0.7	1.2	2.2	8.1×10^{21}	160	210.0	140.0	0.65
S9	14.7 ± 1.4	1.9 ± 0.8	1.0	1.9	1.6×10^{22}	270	330.0	300.0	0.91
S10	11.2 ± 0.7	2.5 ± 0.7	0.3	1.0	1.3×10^{22}	64	40.0	8.4	0.21

Notes. [a] Minor and major axis FWHM values of the Gaussian ellipse, converted to length units. [b] Linear mass density.

In most fields the colour temperature and the spectral index are seen to be anticorrelated, with high spectral indices being found at the location of the temperature minima. The parameters T and β are known to be connected so that any noise present in the observations tends to produce a similar anticorrelation. However, the spatial coherence of the T and β maps strongly suggests that the results of Fig. 3 are not caused by statistical noise. There is still the possibility of systematic errors, but the similarity of the results obtained in separate fields makes this unlikely. A pure calibration error would change the β and T values in a systematic way but would not significantly affect the dispersion of the spectral index values (Juvela et al. 2011). The line-of-sight temperature variations tend to decrease the observed spectral indices. The effect should be stronger toward the cold clump. The fact that β at those positions is larger than in the diffuse areas suggests that the emissivity index of the grains has increased in the cores more than what is visible in the maps, i.e than that inferred from the line-of-sight integrated SEDs (see Malinen et al. 2011). Therefore, the results support the idea of spatial variation of grain properties that could result from temperature-dependent processes in the dust emission mechanism (Meny et al. 2007; Boudet et al. 2005; Coupeaud et al. 2011, see Paper I discussion). We have estimated the effect of the correction of the CO contribution to the 353 GHz fluxes using the CO data survey from Dame et al. (2001), which covers all sources except S2. This has been performed on the SEDs obtained using the large aperture, which is closer to the angular resolution of the CO data. The results lead to a very small change of the fit parameter values, typically with a ∼3% increase of β, and a decrease of the colour temperatures by a few 0.1 K.

4.3. Analysis using ancillary data

4.3.1. *Herschel* and AKARI maps

For all sources we have higher resolution dust continuum data in the form of *Herschel* (resolution 37″ or better) and/or AKARI (58″ or better) maps. These are used: to examine internal structure of the sources; to derive physical parameters of the *Planck* sources and compare them with the results of Sect. 4.1; and to study the properties of the structures found at scales below the *Planck* beam size.

Figure 4 shows *Herschel* 250 μm data (resolution ∼18″) for all, but one, sources. S2 has not been observed with *Herschel* and we show the AKARI 90 μm map instead (∼39″). For comparison, the *Planck* 857 GHz brightness contours are overplotted

and ellipses show the cold clump sizes as derived from elliptical Gaussian fits on the cold residual maps (cf. Paper I and Sect. 3.1.1). A blow-up of the *Herschel* 250 μm maps is shown in Fig. 5.

In most fields, a significant amount of structure at scales below the *Planck* resolution is visible. The Musca field (S10) is an exception. The *Herschel* observations there resolve the filament but do not reveal further structure within the *Planck*-detected clump. Interestingly, this field is among the closest to the Sun. The other filamentary structures (S4, S5, S6, and S7) break up into numerous smaller bright knots, the brightest often coinciding with the position of the *Planck* detection. The two cometary shaped clouds (S1 and S3) similarly harbour a number of bright smaller knots and narrow filaments that show up with a large contrast (>2) above an extended background.

4.3.2. Photometry with *Planck*, *Herschel* and AKARI

We have performed fits on the SEDs of selected substructures within the *Planck* cold clumps to further characterise their inner structure. The aperture photometry is performed after subtraction of a background level estimated as described in Sect. 3. The radius of the largest aperture is 4.5′ (i.e., a diameter of 540″). For the substructures, we use apertures of either 74″ or 116″ diameter. The locations of these apertures are drawn in Fig. 5 and listed in Table 3. The SED fits involve data at wavelengths longer than 100 μm. This removes the problem of a possible contribution from transiently heated grains to the 100 μm flux densities, but also reduces the effects of the line-of-sight temperature variations.

Figure 6 illustrates the various SED estimates for the S1 and S5 fields. It displays the *Planck* SED as given in the C3PO catalogue (therefore corrected for the warm background contribution) and the aperture photometry using smaller apertures on the brightest substructure of the S1 field (Fig. 5). For the large apertures, the flux densities from *Planck* and *Herschel* are in good agreement with each other; in fact it appears that the assumed sources of uncertainty may overestimate the errors. The temperatures obtained for the fixed apertures (Table 3) are the same within the error bars as those derived from the *Planck* and IRIS data only (Table 2). It is therefore most encouraging that the estimates based *only* on *Planck* and IRIS data do not significantly change when the five *Herschel* bands are added that better cover the short wavelength side of the SED maxima. The modified blackbody parameters derived from the fits are listed in Table 3.
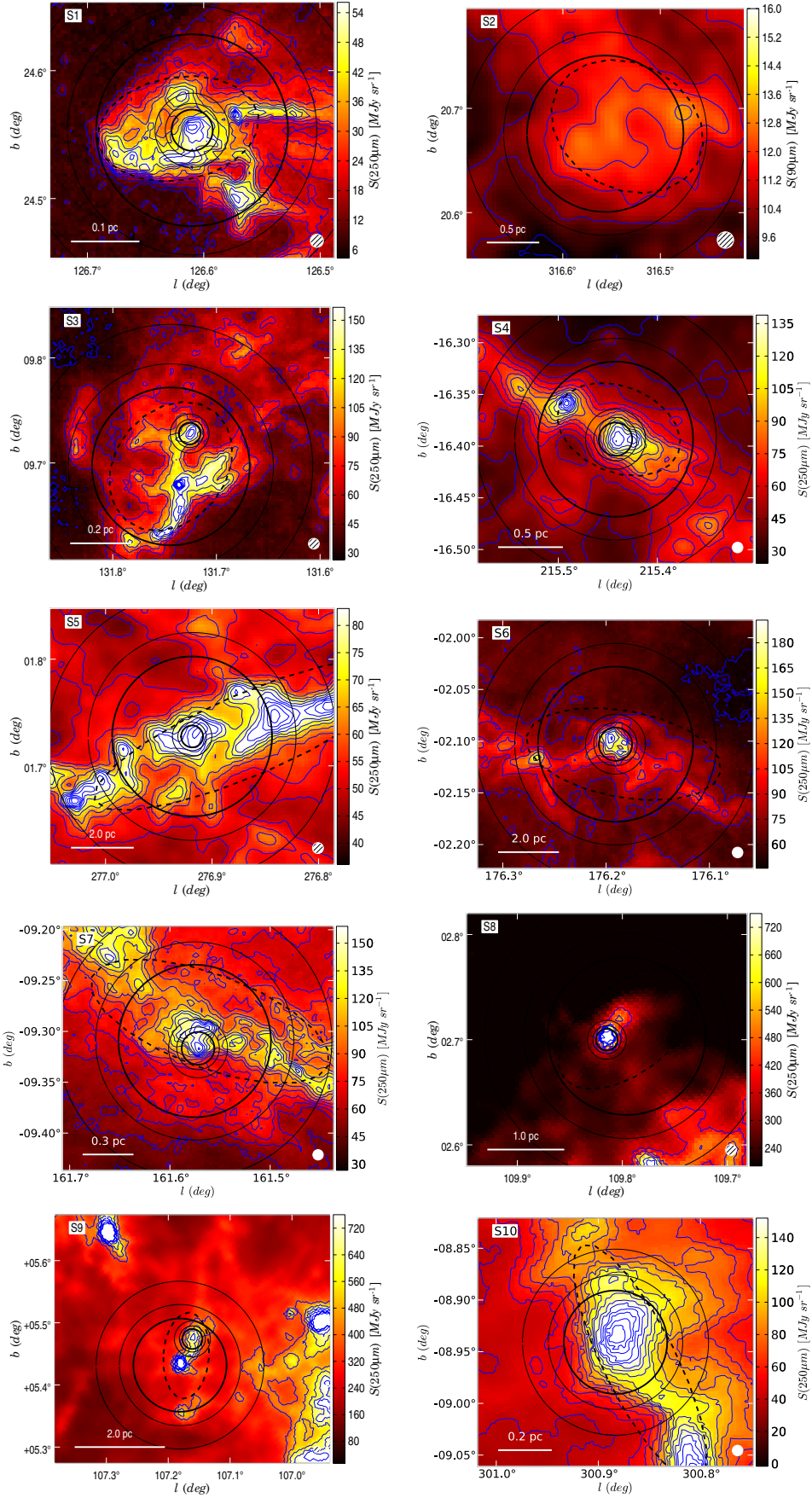
Fig. 5. Blow-up of *Herschel* SPIRE 250 μm maps at the location of the *Planck* cold clumps localised by their elliptic boundary. The different circles and the annuli refer to the apertures adopted for the photometry used in the SEDs. The large aperture has a 9′ diameter, and the smaller ones correspond to either 74″ (S3 and S5), 116″ (S1, S4, S6, S7, S8 and S9), or 360″ (S10).
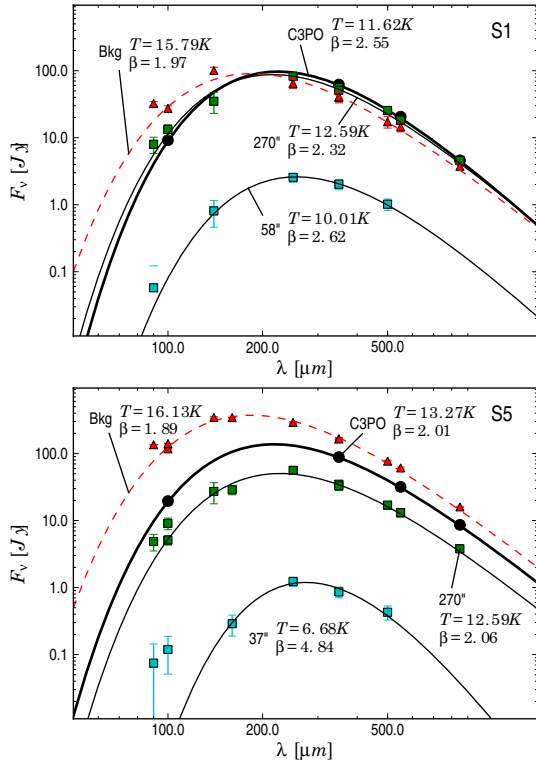
Fig. 6. Spectral energy distribution of various components in the S1 (*upper panel*) and S5 (*lower panel*) fields, including: the *Planck* SED according to the C3PO catalogue (solid circles and thick solid line), aperture photometry with 270″ and 37″ or 58″ radius aperture sizes (squares and thin solid lines) and the background SED (triangles and dashed line). The temperatures and β values derived from the modified blackbody fits are given in the figure (see also Table 3). The background SED is that of the median surface brightness in the reference annulus surrounding the larger aperture (see Fig. 5).

One of the most interesting results is the low temperatures obtained for the SEDs in the 74″ apertures. Except for sources S8 and S9, they are all significantly smaller than those obtained in the larger apertures, the lowest values being at about 7 K. Therefore, in spite of the large telescope beam size, the sensivity of *Planck* is such that the cold clump detection method is actually able to pick-up and locate (within a few arcmin) structures of very cold dust that are significantly smaller than the beam.

In sources S8 and S9, the substructures are found to be warmer, with: $T \sim 19$–21 K. As presented in Juvela et al. (2010), the PACS 100 μm maps have revealed the presence of bright compact sources within the *Planck*-detected clumps. These objects are likely to be very young stellar objects, still embedded in a more extended dense and cold cloud, whose emission is dominating the submillimetre wavelength range studied with *Planck*. As described in the Appendix, S8 and S9 are both located close to active star-forming regions, with S8 having nearby HII regions, and OB stellar associations.

We note that neither S8 or S9 has any clear counterpart in the 100 μm IRAS map (see Figs. A.2 and A.3); the emission of the young stellar objects is not visible, even although this is the same wavelength as for PACS, probably because the sources are very faint, and diluted with the other components in the IRAS beam. However, for S8, both the 170 μm *ISO* Serendipity Survey (Stickel et al. 2007) and the AKARI FIS survey at 140 μm (Doi et al. 2009) showed a faint feature at this position. Shorter wavelength data with higher angular resolution would be

interesting to combine for these particular sources. Among our sample, the field S8 has been observed by *Spitzer*, with the 24 μm MIPS data revealing a number of compact sources. Within the *Planck* clump, the brightest submillimetre peak (PCC288-A in Juvela et al. 2010) is seen to contain at least four distinct midinfrared sources. These data will be analysed in detail in a future publication.

We have also estimated the column densities within each aperture, and the average densities and masses obtained in the smallest aperture. In most cases, the derived column densities are higher than those estimated from the *Planck* clump SEDs. Moreover, as we found with the linear mass densities estimated with *Planck* data, they vary over a factor of about 30. These values should probably be considered as lower limits, because, as shown in Fig. 5, the annulus associated with the small apertures are close to the source and often include a fraction of signal associated with the source itself. We have estimated the impact of the background level on the derived column density by using the average brightness in the largest annulus instead of the smallest. The derived column densities are increased slightly, by up to a factor of 2.

4.3.3. Analysis of molecular line data

All the *Planck* clumps observed in ^{13}CO and C^{18}O lines have a clear line detection, and the small maps show peaks that coincide with the cold substructures (Figs. 7 and 8).

The ^{13}CO linewidths (Table 4) are typically 1–2 km s^{-1} and those of the C^{18}O lines, although narrower, range between 0.3 and 1.6 km s^{-1}. Several velocity components are present, either seen (in a few C^{18}O spectra) as two distinct peaks, or inferred from the non-Gaussian lineshapes, as shown by S6 spectra in Fig. 7. Assuming that the dust and gas in these cold dense clumps is in thermal balance, then the gas temperature is close to 10 K and the sound velocity in CO is low, ~0.05 km s^{-1}. The molecular linewidths are therefore all suprathermal. It is interesting to compare the level of non-thermal support provided by these gas motions to the self-gravity. This can be done by comparing the gas linear mass density with its critical (or virial) value, $m_{vir} = 2\sigma^2/G$ which is the largest mass per unit length of a self-gravitating cylinder, given the non-thermal support provided by the internal motions of dispersion $\sigma = \Delta v/2.35$ (Fiege & Pudritz 2000).

The virial linear mass densities inferred from the C^{18}O linewidths of Table 4 range between 10 $M_\odot$ pc^{-1} for S10, to 260 $M_\odot$ pc^{-1} for S8. A crude comparison with the linear mass densities estimated at the resolution of the *Planck* data (Table 2) suggests that the ratios m/m_{vir} are within a factor of a few of unity. Therefore, as a first approximation, these cold clumps are in rough equilibrium between self-gravity and non-thermal support.

The column densities have been estimated from a single lineof-sight towards each object. When available (in the case of IRAM observations), we have combined the $J = 1 \rightarrow 0$ and $2 \rightarrow 1$ transitions to derive the excitation temperature and the density using a Large Velocity Gradient radiative transfer model (Goldreich & Kwan 1974). In the case of the Onsala and APEX observations, we only have data for one transition; in these cases, we assume an excitation temperature of 11 K and use the C^{18}O line intensity to estimate the column density of the cores. The molecular hydrogen column densities are calculated assuming a C^{18}O fractional abundance of [C^{18}O]/[H$_2$] = 10^{-7}.
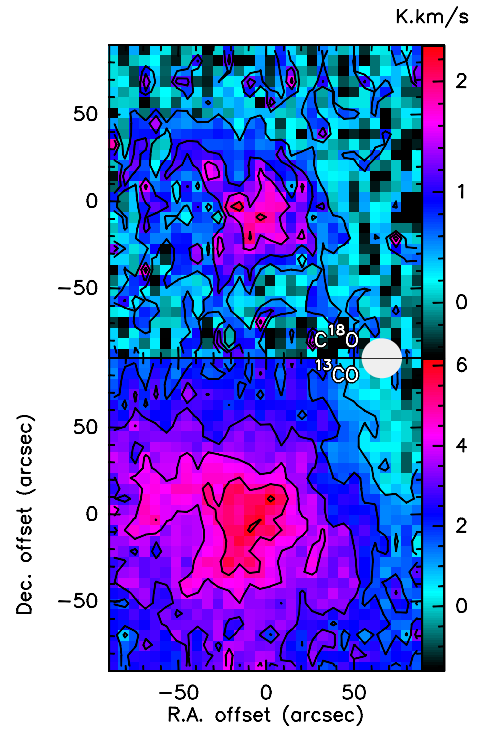
The results are presented in Table 4. The table includes estimates of the mean density, calculated assuming a core size

Table 3. Results from SED fits based on flux densities from aperture photometry (for data at $\lambda > 100\,\mu$m).

Object	l (deg)	b (deg)	Aperture (arcsec)	Aperture size (pc)	T_c (K)	β	N_{H_2} (cm^{-2})	n_{H_2} (cm^{-3})	M ($M_\odot$)
S1-1	126.61	24.55	540	0.39	12.59 ± 0.61	2.32 ± 0.14	9.3×10^{20}		
S1-1	126.61	24.55	116	0.08	10.01 ± 1.32	2.62 ± 0.54	1.9×10^{21}		
S1-1	126.61	24.55	74	0.05	9.75 ± 1.98	2.67 ± 0.92	3.0×10^{21}	2.7×10^4	0.13
S2-1	316.56	20.68	540	1.44	15.08 ± 0.93	1.67 ± 0.17	1.9×10^{20}		
S3-2	131.74	9.70	540	0.52	11.26 ± 0.35	2.36 ± 0.11	3.3×10^{21}		
S3-3	131.74	9.68	116	0.11	7.09 ± 0.74	3.96 ± 0.78	5.3×10^{22}		
S3-4	131.73	9.73	74	0.07	8.53 ± 4.03	3.10 ± 1.03	2.0×10^{22}	1.4×10^5	1.54
S4-1	215.44	−16.39	540	1.18	12.23 ± 0.49	2.18 ± 0.16	1.5×10^{21}		
S4-1	215.44	−16.39	116	0.25	7.02 ± 0.34	4.40 ± 0.42	3.9×10^{22}		
S4-1	215.44	−16.39	74	0.16	7.24 ± 0.80	4.02 ± 0.45	3.2×10^{22}	9.8×10^4	12.4
S5-4	276.92	1.73	540	5.24	12.59 ± 0.28	2.06 ± 0.13	6.1×10^{20}		
S5-4	276.92	1.73	74	0.72	6.68 ± 0.47	4.84 ± 0.11	1.7×10^{22}	1.1×10^4	127.7
S6-2	176.19	−2.10	540	5.24	11.50 ± 0.37	2.31 ± 0.11	1.6×10^{21}		
S6-2	176.19	−2.10	116	1.12	10.78 ± 0.77	1.87 ± 0.51	7.7×10^{21}		
S6-2	176.19	−2.10	74	0.72	10.66 ± 0.62	1.76 ± 0.43	8.0×10^{21}	5.4×10^3	60.0
S7-2	161.57	−9.31	540	0.92	13.63 ± 0.47	2.07 ± 0.12	1.5×10^{21}		
S7-4	161.57	−9.32	116	0.20	13.35 ± 1.13	1.48 ± 0.41	2.4×10^{21}		
S7-4	161.57	−9.32	74	0.13	14.21 ± 1.12	1.19 ± 0.30	1.9×10^{21}	7.5×10^3	0.45
S8-2	109.81	2.70	74	0.29	21.02 ± 2.81	1.29 ± 0.45	5.9×10^{21}	1.0×10^4	7.2
S9-2	107.18	5.43	116	0.45	19.34 ± 2.79	1.44 ± 0.51	6.6×10^{21}	7.1×10^3	19.5
S10-1	300.88	−8.94	360	0.39	11.84 ± 0.65	2.25 ± 0.34	5.4×10^{21}	6.7×10^3	12.2
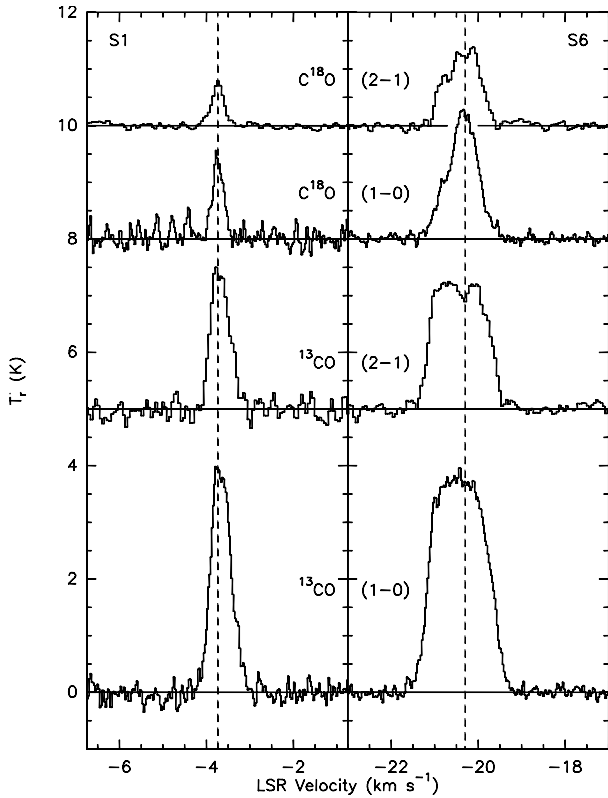
Fig. 7. CO spectral lines from the *Planck* clumps S1 and S6 (taken towards the central positions given in Table 1, and with beam apertures in Table A.1. The spectra are in the antenna temperature scale (T_a^*).

Fig. 8. The S6 source spectral line intensity maps for C^{18}O $J = 1 \rightarrow 0$ (contour steps:0.5 K km s^{-1}, *top image*) and ^{13}CO $J = 1 \rightarrow 0$ (contour steps:1 K km s^{-1}, *bottom image*).The white disk indicates the 30-m HPBW size at the 2.7 mm wavelength, valid for both maps.

corresponding to a diameter of 74″. The column densities are close to the values derived earlier (Table 3) from the dust continuum data, using the smaller aperture sizes (i.e., 74″ or 116″). The estimated average densities of the cores are only of the order of 10^3 cm^{-3}, which is lower than the densities found in nearby dense cores (e.g., Myers et al. 1983). The reason for this is that

C^{18}O is not a good tracer of dense gas because of the significant degree of CO depletion onto dust grains. Within a cold core, the depletion could be almost complete (e.g., Pineda et al. 2010) and so the investigation of this phenomenon towards the *Planck* cores is a natural topic for follow-up studies.

Table 4. CO line parameters for selected lines-of-sight in seven cold core fields.

Target	Telescope	Line	FWHM $(\mathrm{km\,s^{-1}})$	$n_{\mathrm{H_2}}{}^{a}$ $(\mathrm{cm^{-3}})$	$N_{\mathrm{H_2}}{}^{b}$ $(\mathrm{cm^{-2}})$
S1	IRAM	^{12}CO $J = 1 \to 0$	0.71 ± 0.04		
	IRAM	^{12}CO $J = 2 \to 1$	0.78 ± 0.07		
	IRAM	^{13}CO $J = 1 \to 0$	0.53 ± 0.01	3000	3.0×10^{21}
	IRAM	^{13}CO $J = 2 \to 1$	0.50 ± 0.02		
	IRAM	C^{18}O $J = 1 \to 0$	0.30 ± 0.02	2700	4.0×10^{21}
	IRAM	C^{18}O $J = 2 \to 1$	0.32 ± 0.01		
S3	Onsala	^{12}CO $J = 1 \to 0$	2.64 ± 0.03		
	Onsala	^{13}CO $J = 1 \to 0$	1.71 ± 0.04		
	Onsala	C^{18}O $J = 1 \to 0$	1.22 ± 0.08	19000	6.7×10^{21}
S6	IRAM	^{13}CO $J = 1 \to 0$	1.44 ± 0.02		
	IRAM	^{13}CO $J = 2 \to 1$	1.42 ± 0.02		
	IRAM	C^{18}O $J = 1 \to 0$	0.82 ± 0.01	5000	1.4×10^{22}
	IRAM	C^{18}O $J = 2 \to 1$	0.91 ± 0.01		
S7^{c}	IRAM	^{13}CO $J = 1 \to 0$	1.60 ± 0.10		
	IRAM	^{13}CO $J = 2 \to 1$	1.70 ± 0.10		
	IRAM	C^{18}O $J = 1 \to 0$	1.40 ± 0.20	7300	5.6×10^{21}
	IRAM	C^{18}O $J = 2 \to 1$	1.60 ± 0.20		
S8	Onsala	^{13}CO $J = 1 \to 0$	2.06 ± 0.07		
	Onsala	C^{18}O $J = 1 \to 0$	1.82 ± 1.07	6400	1.3×10^{22}
S9A	Onsala	^{13}CO $J = 1 \to 0$	2.54 ± 0.04		
	Onsala	C^{18}O $J = 1 \to 0$	1.57 ± 0.12	25 000	1.8×10^{22}
S9B	Onsala	^{13}CO $J = 1 \to 0$	1.95 ± 0.05		
	Onsala	C^{18}O $J = 1 \to 0$	1.41 ± 0.11	23 000	1.6×10^{22}
S10	APEX	^{12}CO $J = 2 \to 1$	1.39 ± 0.02		
	APEX	^{13}CO $J = 2 \to 1$	0.82 ± 0.03		
	APEX	C^{18}O $J = 2 \to 1$	0.35 ± 0.20	23 000	1.8×10^{22}

Notes. ^{a} Average density along the line of sight. ^{b} Gas column density converted to H_2 column density using the following conversion factors: $N_{\mathrm{H_2}} = 10^6 \times N(^{13}\mathrm{CO})$; and $N_{\mathrm{H_2}} = 10^7 \times N(\mathrm{C^{18}O})$. ^{c} For this source, the lines are an assembly of three components, with strongly asymmetric shapes, which are difficult to analyse separately.

5. Discussion

5.1. The validity of the cold core detection method

A perhaps unexpected result is the physical size of the *Planck* detections. They may have been anticipated to be compact point sources, the result of small cores being diluted within the large beam of *Planck*. However, they are instead found to be significantly extended and elongated, and embedded in filamentary (or cometary) larger-scale structures. As discussed in previous studies, the boundary of a core/clump/cloud structure is always difficult to assess. Curtis & Richer (2010) for instance have shown how much it depends on the method used to identify and extract the core parameters.

In our case, the detection method used to extract sources from the *Planck* data is based on the colour signature of the objects, designed to enable us to detect the cold residuals after the removal of the warmer background. This results in the discovery of a different, more extended cold component with a more complex morphology than sources found with methods that identify structures on the basis of surface brightness (e.g., the "clumpfind" algorithm of Williams et al. (1994), or a multi-scale wavelet analysis). The high sensitivity of *Planck* helps to better separate the warm and cold components, particularly in combination with data at somewhat shorter wavelengths.

The faint, mostly filamentary, emission of cold dust that we detect here could perhaps be called a "cold matrix" linking the

substructures to each other over a broad range of scales. By combining *Planck* and *Herschel* it is possible to probe in detail the link between 10-pc scale filamentary structures and sub-parsec scale cold cores. Future studies with much larger samples should bring new insights to the origin of the cores and the mechanisms associated with their formation.

5.2. The limitations of the SED fitting

One has to be careful not to over-interpret SED fits based on a modified blackbody function, with a single colour temperature and optical depth. In reality the ISM has a broad distribution of dust temperatures and opacities (as well as column densities), within a *Planck* beam. Shetty et al. (2009) have discussed in detail the biases introduced by line-of-sight temperature variations and noise in the interpretation of such SED fits. Our study suggests that we are not badly contaminated by these effects for several reasons. Firstly Planck's broad spectral coverage, combined with IRIS allows us to determining both the dust temperature and emissivity spectral index. And secondly, we stress that the cold core detection method identifies structures where the submillimetre SED is dominated by localised dust emission colder than its large scale background.

An indirect indication that the parameters derived from the SEDs fits are not strongly biased is that the physical properties inferred cover the range of values known to be those of prestellar cores. Such cores have different properties whether they belong to regions of low- or high-mass star formation. Their column densities range between a few times 10^{21} or 10^{22} cm^{-2} in nearby star forming regions (Motte et al. 1998; Kauffmann et al. 2008; Enoch et al. 2006, 2007; Hatchell et al. 2005; Curtis & Richer 2010; André et al. 2010) to $\sim 10^{23}$ cm^{-2} in the cores of infrared dark clouds (IRDCs, Simon et al. 2006; Rathborne et al. 2010; Peretto et al. 2010). These IRDCs, discovered by means of mid-infrared absorption towards the bright background emission of the Galactic Plane (*MSX* and ISOGAL surveys, Egan et al. 1998; Perault et al. 1996), are thought to be the sites of formation of massive stars and star clusters (Rathborne et al. 2006). The inferred average densities depend on their size, which ranges between <0.1 pc for low-mass dense cores of ~1 $M_{\odot}$, to 0.5 pc or more for ~10^3 $M_{\odot}$ IRDC cores. Our *Planck* cold clumps subsample is not located within the *MSX* IRDCs spatial distribution, so we cannot compare them directly with any IRDC association. However, the properties we derive fall well within this range. It is noteworthy that the *Planck* cold clumps are elongated structures which tend to exist within extended filaments (up to 30 pc in the present subsample), with thickness up to ~3 pc. The IRDCs identified as extinction peaks in mid-infrared maps have similar lengthscales and column densities, but they are usually thinner and therefore have higher densities. It is also interesting that the linear mass densities of the filaments in which the *Planck* cold clumps are embedded cover the same range as the warm filamentary structures associated with active star-forming regions, i.e., extending up to several 100 $M_{\odot}$ pc^{-1}.

The temperatures derived in the sample studied here cover a range (10–14.5 K) similar to previous estimates on a number of cold condensations detected using multi-wavelength submillimetre observations with the balloon-borne experiments: PRONAOS, $T \sim 12$ K in star-forming and cirrus regions (Stepnik et al. 2003; Dupac et al. 2003; Bernard et al. 1999); Archeops, 7–18 K (Désert et al. 2008); and BLAST, 9–14 K (Netterfield et al. 2009). These temperatures are all lower, however, than those measured in the so-called "quiescent" IRDC cores (Rathborne et al. 2010) that span from 17 to 30 K for a similar range in

column density (0.3–3×10^{22} cm^{-2}) and mass (10–$10^3\,M_\odot$). The *Planck* cold clump population may therefore be representative of a still earlier stage of evolution of cold dense cores.

6. Summary and perspectives

We have presented a preliminary analysis of a sample of 10 sources from the C3PO catalogue in order to illustrate and better probe the nature and properties of the cold objects detected with *Planck*. The sources have been chosen to span a broad range in temperature, density, mass and morphology (inluding filaments and isolated/clustered structures) in a variety of environments, from star-forming regions (both remote and nearby), to high Galactic latitude cirrus clouds. The main findings are as follows:

1. The sources are significantly larger than the *Planck* beam, with elongated shapes, and appear to belong to filamentary structures, with lengths up to 20 pc;
2. The physical parameters of the sources have been derived from SEDs by combining *Planck* (HFI bands at 857, 545, and 353 GHz) and IRIS data, finding $T \sim 10$–15 K (with a mean value of 12.4 K), $\beta \sim 1.8$–2.5 (mean 2.2) and $N_{H_2} \sim 0.8$–16×10^{21} cm^{-2}, from which we infer linear mass densities in the range $m = 15$–$400\,M_\odot$ pc^{-1}, masses $M \sim 3.5$–$1800\,M_\odot$, bolometric luminosities $L \sim 1$–$300\,L_\odot$, and $L/M \sim 0.1$–$0.9\,L_\odot/M_\odot$;
3. Except for the faintest source (which lies at high Galactic latitude), a clear signature of cold dust emission is visible directly in the $1° \times 1°$ maps of dust temperature, spectral index and column density, with colour temperatures of typically ~ 14 K, surrounded by a warmer extended (often elongated) emission at around 16–18 K;
4. *Herschel* and AKARI observations at higher angular resolution have revealed a rich and complex substructure within the *Planck* clumps, in most cases the substructures being colder (down to 7 K) than the *Planck*-detected clumps, although in two cases, the substructures are warmer because they harbour compact infrared objects, likely protostellar sources at an early stage;
5. Molecular line observations of 7 of the sources show that all of them are clearly detected in ^{13}CO and C^{18}O, ^{13}CO linewidths typically 1–2 km s^{-1}, and C^{18}O lines always narrower (down to ~ 0.3 km s^{-1}) but still clearly suprathermal, given the anticipated low temperature of the gas, suggesting that the support of *Planck* cold clumps against self-gravity is dominated by non-thermal motions.

Although we have focussed here on a very small sample of 10 clumps, the results are indicative of what might be expected from the more ambitious studies which will follow. We have already shown that the C3PO list of *Planck* cold sources contains objects with a wide variety of physical properties. These are probably associated with different evolutionary stages of the star formation process, from quiescent, cold and starless clumps, through prestellar stages to very young protostellar objects still embedded in their cold surrounding cloud. Forthcoming papers will present a more detailed analysis of the sources using *Herschel* data combined with *Planck* for larger and more statistically robust samples. More detailed physical modelling will allow for characterisation of clustering and fragmentation within the *Planck* clumps, addressing the question of their evolutionary stage, along with the study of stability of the starless substructures.

The first unbiased all-sky catalogue of cold objects provided by *Planck* offers the opportunity to investigate the properties of the population of Galactic cold objects over the entire sky. The full sample will include objects at the very early stages of evolution, in a variety of large-scale environments, and in particular, outside the well-known molecular complexes, at high latitude or at large distances within the Galactic Plane. For this purpose, dedicated follow-up observations are needed in both higher resolution continuum mode and spectroscopy, which is the objective of the "Galactic Cold Cores" key programme, planning a follow-up with PACS and SPIRE of about 300 *Planck* cold clumps. In parallel, similar and/or complementary follow-up studies will be possible on the basis of the ECC catalogue which has been delivered to the astronomical community, providing a robust subsample of the C3PO catalogue, with more than 900 *Planck* cold clumps distributed over the whole sky.

References

André, P., Men'shchikov, A., Bontemps, S., et al. 2010, A&A, 518, L102
Beckwith, S. V. W., Sargent, A. I., Chini, R. S., & Guesten, R. 1990, AJ, 99, 924
Bensch, F., Leuenhagen, U., Stutzki, J., & Schieder, R. 2003, ApJ, 591, 1013
Bergin, E. A., & Tafalla, M. 2007, ARA&A, 45, 339
Bernard, J. P., Abergel, A., Ristorcelli, I., et al. 1999, A&A, 347, 640
Bersanelli, M., Mandolesi, N., Butler, R. C., et al. 2010, A&A, 520, A4
Boden, K., & Heithausen, A. 1993, A&A, 268, 255
Bontemps, S., André, P., Könyves, V., et al. 2010, A&A, 518, L85
Boudet, N., Mutschke, H., Nayral, C., et al. 2005, ApJ, 633, 272
Boulanger, F., Abergel, A., Bernard, J., et al. 1996, A&A, 312, 256
Bourke, T. L., Hyland, A. R., & Robinson, G. 1995, MNRAS, 276, 1052
Cantalupo, C. M., Borrill, J. D., Jaffe, A. H., Kisner, T. S., & Stompor, R. 2010, ApJS, 187, 212
Compiègne, M., Flagey, N., Noriega-Crespo, A., et al. 2010, ApJ, 724, L44
Coupeaud, A., Demyk, K., Meny, C., & Nayral, C. 2011, in IAU Symp., 280, 138
Crutcher, R. M., Hakobian, N., & Troland, T. H. 2009, ApJ, 692, 844
Curtis, E. I., & Richer, J. S. 2010, MNRAS, 402, 603
Dame, T. M., Hartmann, D., & Thaddeus, P. 2001, ApJ, 547, 792
Désert, F., Macías-Pérez, J. F., Mayet, F., et al. 2008, A&A, 481, 411
di Francesco, J., Sadavoy, S., Motte, F., et al. 2010, A&A, 518, L91
Dobashi, K., Uehara, H., Kandori, R., et al. 2005, PASJ, 57, 1
Doi, Y., Etxaluze Azkonaga, M., White, G., et al. 2009, in The Next-Generation Infrared Space Mission: SPICA, ed. A. M. Heras, B. M. Swinyard, K. G. Isaak, & J. R. Goicoechea, 4018
Dupac, X., Bernard, J., Boudet, N., et al. 2003, A&A, 404, L11
Egan, M. P., Shipman, R. F., Price, S. D., et al. 1998, ApJ, 494, L199
Enoch, M. L., Young, K. E., Glenn, J., et al. 2006, ApJ, 638, 293
Enoch, M. L., Glenn, J., Evans, II, N. J., et al. 2007, ApJ, 666, 982
Falgarone, E., Pety, J., & Phillips, T. G. 2001, ApJ, 555, 178
Fiege, J. D., & Pudritz, R. E. 2000, ApJ, 534, 291
Fukui, Y., Mizuno, N., Yamaguchi, R., et al. 1999, PASJ, 51, 745
Goldreich, P., & Kwan, J. 1974, ApJ, 189, 441
Górski, K. M., Hivon, E., Banday, A. J., et al. 2005, ApJ, 622, 759
Goss, W. M., Manchester, R. N., Brooks, J. W., et al. 1980, MNRAS, 191, 533
Griffin, M. J., Abergel, A., Abreu, A., et al. 2010, A&A, 518, L3

Haikala, L. K., Juvela, M., Harju, J., et al. 2006, A&A, 454, L71
Hatchell, J., Richer, J. S., Fuller, G. A., et al. 2005, A&A, 440, 151
Heithausen, A., & Thaddeus, P. 1990, ApJ, 353, L49
Henning, T., Michel, B., & Stognienko, R. 1995, Planet. Space Sci., 43, 1333
Hily-Blant, P., Falgarone, E., Pineau Des Forêts, G., & Phillips, T. G. 2004, Ap&SS, 292, 285
Johnstone, D., Wilson, C. D., Moriarty-Schieven, G., et al. 2000, ApJ, 545, 327
Jordi, C., Trullols, E., & Galadi-Enriquez, D. 1996, A&A, 312, 499
Juvela, M., Ristorcelli, I., Montier, L. A., et al. 2010, A&A, 518, L93
Juvela, M., Ristorcelli, I., Pelkonen, V.-M., et al. 2011, A&A, 527, A111
Kauffmann, J., Bertoldi, F., Bourke, T. L., Evans, II, N. J., & Lee, C. W. 2008, A&A, 487, 993
Könyves, V., André, P., Men'shchikov, A., et al. 2010, A&A, 518, L106
Kramer, C., Stutzki, J., Rohrig, R., & Corneliussen, U. 1998, A&A, 329, 249
Kruegel, E., & Siebenmorgen, R. 1994, A&A, 288, 929
Lamarre, J., Puget, J., Ade, P. A. R., et al. 2010, A&A, 520, A9
Leahy, J. P., Bersanelli, M., D'Arcangelo, O., et al. 2010, A&A, 520, A8
Liseau, R., Lorenzetti, D., Nisini, B., Spinoglio, L., & Moneti, A. 1992, A&A, 265, 577
Lombardi, M., & Alves, J. 2001, A&A, 377, 1023
Lynds, B. T. 1965, ApJS, 12, 163
Maheswar, G., Manoj, P., & Bhatt, H. C. 2004, MNRAS, 355, 1272
Malinen, J., Juvela, M., Collins, D. C., Lunttila, T., & Padoan, P. 2011, A&A, 530, A101
Mandolesi, N., Bersanelli, M., Butler, R. C., et al. 2010, A&A, 520, A3
Marshall, D. J., Robin, A. C., Reylé, C., Schultheis, M., & Picaud, S. 2006, A&A, 453, 635
McKee, C. F., & Ostriker, E. C. 2007, ARA&A, 45, 565
Mennella, A., Butler, R. C., Curto, A., et al. 2011, A&A, 536, A3
Men'shchikov, A., André, P., Didelon, P., et al. 2010, A&A, 518, L103
Meny, C., Gromov, V., Boudet, N., et al. 2007, A&A, 468, 171
Mitra, S., Rocha, G., Górski, K. M., et al. 2011, ApJS, 193, 5
Miville-Deschênes, M., & Lagache, G. 2005, ApJS, 157, 302
Molinari, S., Swinyard, B., Bally, J., et al. 2010, A&A, 518, L100
Montier, L. A., Pelkonen, V., Juvela, M., Ristorcelli, I., & Marshall, D. J. 2010, A&A, 522, A83
Motte, F., Andre, P., & Neri, R. 1998, A&A, 336, 150
Motte, F., Bontemps, S., Schilke, P., et al. 2007, A&A, 476, 1243
Motte, F., Zavagno, A., Bontemps, S., et al. 2010, A&A, 518, L77
Murakami, H., Baba, H., Barthel, P., et al. 2007, PASJ, 59, 369
Murphy, D. C., & May, J. 1991, A&A, 247, 202
Myers, P. C., Linke, R. A., & Benson, P. J. 1983, ApJ, 264, 517
Netterfield, C. B., Ade, P. A. R., Bock, J. J., et al. 2009, ApJ, 707, 1824
Obayashi, A., Kun, M., Sato, F., Yonekura, Y., & Fukui, Y. 1998, AJ, 115, 274
Olmi, L., Ade, P. A. R., Anglés-Alcázar, D., et al. 2009, ApJ, 707, 1836
Ossenkopf, V., & Henning, T. 1994, A&A, 291, 943
Otrupcek, R. E., Hartley, M., & Wang, J. 2000, PASA, 17, 92
Pagani, L., Daniel, F., & Dubernet, M. 2009, A&A, 494, 719
Perault, M., Omont, A., Simon, G., et al. 1996, A&A, 315, L165
Peretto, N., Fuller, G. A., Plume, R., et al. 2010, A&A, 518, L98
Pilbratt, G. L., Riedinger, J. R., Passvogel, T., et al. 2010, A&A, 518, L1
Pineda, J. L., Goldsmith, P. F., Chapman, N., et al. 2010, ApJ, 721, 686
Planck Collaboration 2011a, A&A, 536, A1
Planck Collaboration 2011b, A&A, 536, A2
Planck Collaboration 2011c, A&A, 536, A7
Planck Collaboration 2011d, A&A, 536, A8
Planck Collaboration 2011e, A&A, 536, A9
Planck Collaboration 2011f, A&A, 536, A10
Planck Collaboration 2011g, A&A, 536, A11
Planck Collaboration 2011h, A&A, 536, A12
Planck Collaboration 2011i, A&A, 536, A13
Planck Collaboration. 2011j, A&A, 536, A14
Planck Collaboration 2011k, A&A, 536, A15
Planck Collaboration 2011l, A&A, 536, A16
Planck Collaboration 2011m, A&A, 536, A17
Planck Collaboration 2011n, A&A, 536, A18
Planck Collaboration 2011o, A&A, 536, A19
Planck Collaboration 2011p, A&A, 536, A20
Planck Collaboration 2011q, A&A, 536, A21
Planck Collaboration 2011r, A&A, 536, A22
Planck Collaboration 2011s, A&A, 536, A23
Planck Collaboration 2011t, A&A, 536, A24
Planck Collaboration 2011u, A&A, 536, A25
Planck Collaboration 2011v, The Explanatory Supplement to the Planck Early Release Compact Source Catalogue (ESA)
Planck Collaboration 2011w, A&A, 536, A26
Planck HFI Core Team 2011a, A&A, 536, A4
Planck HFI Core Team 2011b, A&A, 536, A6

Poglitsch, A., Waelkens, C., Geis, N., et al. 2010, A&A, 518, L2
Preibisch, T., Ossenkopf, V., Yorke, H. W., & Henning, T. 1993, A&A, 279, 577
Rathborne, J. M., Jackson, J. M., & Simon, R. 2006, ApJ, 641, 389
Rathborne, J. M., Jackson, J. M., Chambers, E. T., et al. 2010, ApJ, 715, 310
Rosset, C., Tristram, M., Ponthieu, N., et al. 2010, A&A, 520, A13
Roy, A., Ade, P. A. R., Bock, J. J., et al. 2011, ApJ, 730, 142
Sargent, A. I. 1977, ApJ, 218, 736
Schlegel, D. J., Finkbeiner, D. P., & Davis, M. 1998, ApJ, 500, 525
Schneider, N., Motte, F., Bontemps, S., et al. 2010, A&A, 518, L83
Shetty, R., Kauffmann, J., Schnee, S., Goodman, A. A., & Ercolano, B. 2009, ApJ, 696, 2234
Simon, R., Rathborne, J. M., Shah, R. Y., Jackson, J. M., & Chambers, E. T. 2006, ApJ, 653, 1325
Skrutskie, M., Cutri, R., Stiening, R., et al. 2006, AJ, 131, 1163, owner: marshall Added to JabRef: 2008.07.29
Stepnik, B., Abergel, A., Bernard, J., et al. 2003, A&A, 398, 551
Stickel, M., Krause, O., Klaas, U., & Lemke, D. 2007, A&A, 466, 1205
Stutz, A., Launhardt, R., Linz, H., et al. 2010, A&A, 518, L87
Tafalla, M., Bachiller, R., & Martin-Pintado, J. 1993, ApJ, 403, 175
Tauber, J. A., Mandolesi, N., Puget, J., et al. 2010, A&A, 520, A1
Ungerechts, H., & Thaddeus, P. 1987, ApJS, 63, 645
van Till, H., Loren, R., & Davis, J. 1975, ApJ, 198, 235
Vilas-Boas, J. W. S., Myers, P. C., & Fuller, G. A. 1994, ApJ, 433, 96
Ward-Thompson, D., André, P., Crutcher, R., et al. 2007, Protostars and Planets V, 33
Ward-Thompson, D., Kirk, J. M., André, P., et al. 2010, A&A, 518, L92
White, G. J. 1993, A&A, 274, L33
Williams, J. P., de Geus, E. J., & Blitz, L. 1994, ApJ, 428, 693
Williams, J. P., Blitz, L., & McKee, C. F. 2000, Protostars and Planets IV, 97
Yamamura, I. 2008, in COSPAR, Plenary Meeting, 37th COSPAR Scientific Assembly, 37, 3529
Yonekura, Y., Mizuno, N., Saito, H., et al. 1999, PASJ, 51, 911
Zacchei, A., Maino, D., Baccigalupi, C., et al. 2011, A&A, 536, A5
Zavagno, A., Russeil, D., Motte, F., et al. 2010, A&A, 518, L81

[1] Aalto University Metsähovi Radio Observatory, Metsähovintie 114, 02540 Kylmälä, Finland

[2] Agenzia Spaziale Italiana Science Data Center, c/o ESRIN, Via Galileo Galilei, Frascati, Italy

[3] Astroparticule et Cosmologie, CNRS (UMR7164), Université Denis Diderot Paris 7, Bâtiment Condorcet, 10 rue A. Domon et Léonie Duquet, Paris, France

[4] Astrophysics Group, Cavendish Laboratory, University of Cambridge, JJ Thomson Avenue, Cambridge CB3 0HE, UK

[5] Atacama Large Millimeter/submillimeter Array, ALMA Santiago Central Offices, Alonso de Cordova 3107, Vitacura, Casilla 763 0355, Santiago, Chile

[6] CITA, University of Toronto, 60 St. George St., Toronto, ON M5S 3H8, Canada

[7] CNRS, IRAP, 9 Av. colonel Roche, BP 44346, 31028 Toulouse Cedex 4, France

[8] California Institute of Technology, Pasadena, California, USA

[9] DAMTP, University of Cambridge, Centre for Mathematical Sciences, Wilberforce Road, Cambridge CB3 0WA, UK

[10] DSM/Irfu/SPP, CEA-Saclay, 91191 Gif-sur-Yvette Cedex, France

[11] DTU Space, National Space Institute, Juliane Mariesvej 30, Copenhagen, Denmark

[12] Departamento de Física, Universidad de Oviedo, Avda. Calvo Sotelo s/n, Oviedo, Spain

[13] Department of Astronomy and Astrophysics, University of Toronto, 50 Saint George Street, Toronto, Ontario, Canada

[14] Department of Earth Sciences and Astronomy, University of Tokyo, Komaba 3-8-1, Meguro, Tokyo 153-8902, Japan

[15] Department of Physics & Astronomy, University of British Columbia, 6224 Agricultural Road, Vancouver, British Columbia, Canada

[16] Department of Physics, Gustaf Hällströmin katu 2a, University of Helsinki, Helsinki, Finland

[17] Department of Physics, Princeton University, Princeton, New Jersey, USA

[18] Department of Physics, Purdue University, 525 Northwestern Avenue, West Lafayette, Indiana, USA

[19] Department of Physics, University of California, Berkeley, California, USA

[20] Department of Physics, University of California, One Shields Avenue, Davis, California, USA

[21] Department of Physics, University of California, Santa Barbara, California, USA

[22] Department of Physics, University of Illinois at Urbana-Champaign, 1110 West Green Street, Urbana, Illinois, USA

[23] Dipartimento di Fisica G. Galilei, Università degli Studi di Padova, Via Marzolo 8, 35131 Padova, Italy

[24] Dipartimento di Fisica, Università La Sapienza, P.le A. Moro 2, Roma, Italy

[25] Dipartimento di Fisica, Università degli Studi di Milano, Via Celoria, 16, Milano, Italy

[26] Dipartimento di Fisica, Università degli Studi di Trieste, Via A. Valerio 2, Trieste, Italy

[27] Dipartimento di Fisica, Università di Ferrara, Via Saragat 1, 44122 Ferrara, Italy

[28] Dipartimento di Fisica, Università di Roma Tor Vergata, Via della Ricerca Scientifica 1, Roma, Italy

[29] Discovery Center, Niels Bohr Institute, Blegdamsvej 17, Copenhagen, Denmark

[30] Dpto. Astrofísica, Universidad de La Laguna (ULL), 38206 La Laguna, Tenerife, Spain

[31] Eötvös Loránd University, Department of Astronomy, Pázmány Péter sétány 1/A, 1117 Budapest, Hungary

[32] European Southern Observatory, ESO Vitacura, Alonso de Cordova 3107, Vitacura, Casilla 19001, Santiago, Chile

[33] European Space Agency, ESAC, Planck Science Office, Camino bajo del Castillo s/n, Urbanización Villafranca del Castillo, Villanueva de la Cañada, Madrid, Spain

[34] European Space Agency, ESTEC, Keplerlaan 1, 2201 AZ Noordwijk, The Netherlands

[35] Helsinki Institute of Physics, Gustaf Hällströmin katu 2, University of Helsinki, Helsinki, Finland

[36] INAF - Osservatorio Astrofisico di Catania, Via S. Sofia 78, Catania, Italy

[37] INAF - Osservatorio Astronomico di Padova, Vicolo dell'Osservatorio 5, Padova, Italy

[38] INAF - Osservatorio Astronomico di Roma, Via di Frascati 33, Monte Porzio Catone, Italy

[39] INAF - Osservatorio Astronomico di Trieste, Via G.B. Tiepolo 11, Trieste, Italy

[40] INAF/IASF Bologna, Via Gobetti 101, Bologna, Italy

[41] INAF/IASF Milano, Via E. Bassini 15, Milano, Italy

[42] INRIA, Laboratoire de Recherche en Informatique, Université Paris-Sud 11, Bâtiment 490, 91405 Orsay Cedex, France

[43] IPAG (Institut de Planétologie et d'Astrophysique de Grenoble), Université Joseph Fourier, Grenoble 1/CNRS-INSU, UMR 5274, 38041 Grenoble, France

[44] Imperial College London, Astrophysics group, Blackett Laboratory, Prince Consort Road, London, SW7 2AZ, UK

[45] Infrared Processing and Analysis Center, California Institute of Technology, Pasadena, CA 91125, USA

[46] Institut Néel, CNRS, Université Joseph Fourier Grenoble I, 25 rue des Martyrs, Grenoble, France

[47] Institut d'Astrophysique Spatiale, CNRS (UMR8617) Université Paris-Sud 11, Bâtiment 121, Orsay, France

[48] Institut d'Astrophysique de Paris, CNRS UMR7095, Université Pierre & Marie Curie, 98bis boulevard Arago, Paris, France

[49] Institute of Astronomy and Astrophysics, Academia Sinica, Taipei, Taiwan

[50] Institute of Astronomy, University of Cambridge, Madingley Road, Cambridge CB3 0HA, UK

[51] Institute of Space and Astronautical Science, Japan Aerospace Exploration Agency, 3-1-1 Yoshinodai, Chuo-ku, Sagamihara, Kanagawa, 252-5210, Japan

[52] Institute of Theoretical Astrophysics, University of Oslo, Blindern, Oslo, Norway

[53] Instituto de Astrofísica de Canarias, C/Vía Láctea s/n, La Laguna, Tenerife, Spain

[54] Instituto de Física de Cantabria (CSIC-Universidad de Cantabria), Avda. de los Castros s/n, Santander, Spain

[55] Jet Propulsion Laboratory, California Institute of Technology, 4800 Oak Grove Drive, Pasadena, California, USA

[56] Jodrell Bank Centre for Astrophysics, Alan Turing Building, School of Physics and Astronomy, The University of Manchester, Oxford Road, Manchester M13 9PL, UK

[57] Kavli Institute for Cosmology Cambridge, Madingley Road, Cambridge CB3 0HA, UK

[58] LERMA, CNRS, Observatoire de Paris, 61 avenue de l'Observatoire, Paris, France

[59] Laboratoire AIM, IRFU/Service d'Astrophysique - CEA/DSM - CNRS - Université Paris Diderot, Bât. 709, CEA-Saclay, 91191 Gif-sur-Yvette Cedex, France

[60] Laboratoire Traitement et Communication de l'Information, CNRS (UMR 5141) and Télécom ParisTech, 46 rue Barrault, 75634 Paris Cedex 13, France

[61] Laboratoire de Physique Subatomique et de Cosmologie, CNRS/IN2P3, Université Joseph Fourier Grenoble I, Institut National Polytechnique de Grenoble, 53 rue des Martyrs, 38026 Grenoble Cedex, France

[62] Laboratoire de l'Accélérateur Linéaire, Université Paris-Sud 11, CNRS/IN2P3, Orsay, France

[63] Lawrence Berkeley National Laboratory, Berkeley, California, USA

[64] Max-Planck-Institut für Astrophysik, Karl-Schwarzschild-Str. 1, 85741 Garching, Germany

[65] MilliLab, VTT Technical Research Centre of Finland, Tietotie 3, Espoo, Finland

[66] National University of Ireland, Department of Experimental Physics, Maynooth, Co. Kildare, Ireland

[67] Niels Bohr Institute, Blegdamsvej 17, Copenhagen, Denmark

[68] Observational Cosmology, Mail Stop 367-17, California Institute of Technology, Pasadena, CA, 91125, USA

[69] Optical Science Laboratory, University College London, Gower Street, London, UK

[70] SISSA, Astrophysics Sector, Via Bonomea 265, 34136 Trieste, Italy

[71] SUPA, Institute for Astronomy, University of Edinburgh, Royal Observatory, Blackford Hill, Edinburgh EH9 3HJ, UK

[72] School of Physics and Astronomy, Cardiff University, Queens Buildings, The Parade, Cardiff CF24 3AA, UK

[73] Space Sciences Laboratory, University of California, Berkeley, California, USA

[74] Spitzer Science Center, 1200 E. California Blvd., Pasadena, California, USA

[75] Stanford University, Dept of Physics, Varian Physics Bldg, 382 Via Pueblo Mall, Stanford, California, USA

[76] Université de Toulouse, UPS-OMP, IRAP, 31028 Toulouse Cedex 4, France

[77] Universities Space Research Association, Stratospheric Observatory for Infrared Astronomy, MS 211-3, Moffett Field, CA 94035, USA

[78] University of Granada, Departamento de Física Teórica y del Cosmos, Facultad de Ciencias, Granada, Spain

[79] University of Miami, Knight Physics Building, 1320 Campo Sano Dr., Coral Gables, Florida, USA

[80] Warsaw University Observatory, Aleje Ujazdowskie 4, 00-478 Warszawa, Poland

Appendix A: Selected sources, illustration of detection method, source elongation and observational parameters

We list below the main features of the selected fields as known based on previous studies.

S1 lies in a tenuous high-latitude cloud, MCLD 126.5+24.5, located at the border of the Polaris Flare, a large molecular cirrus cloud in the direction of the north celestial pole (Heithausen & Thaddeus 1990), at an estimated distance of 150 pc (Bensch et al. 2003). The cloud was first noted from the POSS prints by Lynds (1965) as the small reflection nebula LBN 628. Its cometary globule shape appears similar to what is usually found in active star formation regions, although this nebula is far from any such region. Boden & Heithausen (1993) have studied the gas properties of the densest part of the cloud, observing transition lines of the dense tracors ^{12}CO, ^{13}CO, H_2CO, and NH_3. The ammonia core (~ 0.14 pc $\times 0.07$ pc) corresponds to $0.2\ M_\odot$ and a density of 4000 cm^{-3}. Although this density is high compared to the cirrus-like environment, Boden & Heithausen (1993) find that both the cloud and the core are probably gravitationally unbound. The line ratios found are consistent with shocked gas being compressed by the North Celestial Pole H I loop (Kramer et al. 1998).

S2 is embedded in the tail ($\sim 30'$ south) of the well-studied cometary globule CG12. This isolated globule is located at high Galactic latitude ($l = 316.5°$, $b = 21.2°$), with a $1°$ long nebular tail nearly perpendicular to the Galactic Plane. Its distance of 550 pc has been determined using a photometry-extinction method by Maheswar et al. (2004). Molecular studies using ^{12}CO (van Till et al. 1975; White 1993; Yonekura et al. 1999), $C^{18}O$ (Haikala et al. 2006), H_2CO (Goss et al. 1980) and NH_3 (Bourke et al. 1995) reveal star formation activity, with the presence of a highly collimated bipolar outflow in the head of the cloud. CG12 seems to be a rare example of triggered star formation at relatively large Galactic height (Maheswar et al. 2004).

S3 is located in the constellation of Cassiopeia and has no counterpart in the SIMBAD database. On the sky, the closest Lynds catalogue sources are LDN 1358 and LDN 1355, which are, respectively, at distances of 114 and 118'. These Lynds sources are associated with the Cepheus flare at a distance of 200 ± 50 pc (Obayashi et al. 1998; Kauffmann et al. 2008). The *Planck* detection is associated with an AKARI FIS bright source catalogue source that has a cirrus type spectrum (Yamamura 2008).

S4 is in the Orion region, within a dark cloud that was mapped by Dobashi et al. (2005) in extinction, derived from Digitized Sky Survey images. The source is located six degrees east of the M42 nebula, in the Dobashi et al. cloud 1490, close to its clump P43. It has not been the subject of any dedicated studies, so far. In higher resolution extinction images derived from the colour excess of 2MASS stars, the cloud is seen to reside within a narrow filament. In the *Planck* data, the filament is clearly visible, but remains unresolved. The source itself is a compact, slightly elongated clump that stands out just as well in the individual *Planck* frequency maps as in the cold residual map. The Nanten CO data show a peak at the same position, with a line intensity close to 20 K km s^{-1}.

S5 is a filamentary structure located near the Vela Molecular Ridge (hereafter VMR), a giant molecular cloud complex in the outer Galaxy. Murphy & May (1991) mapped the VMR in CO, but the mapping did not cover S5. However, Otrupcek et al. (2000) carried out CO observations of the dark cloud DCld 276.9+01.7, with angular extent of 16' by 3', and this is

interposed on the filament. The detected CO line is rather strong ($T_A^* = 6.1$ K), with a velocity (relative to the local standard of rest) of ~ 2 km s^{-1}. We derive a kinematic distance for the cloud of ~ 2 kpc. This is consistent with the distance estimate of the VMR: Liseau et al. (1992) give a photometric distance of (0.7 ± 0.2) kpc for parts A, C and D of the VMR and 2 kpc for part B, using the nomenclature established by Murphy & May (1991) and agreeing with their results. Thus we consider it is likely that S5 is part of the VMR. Several studies have been published on the VMR young star-forming region, for example, Olmi et al. (2009) found 141 BLAST cores (starless and protostellar) in the Vela-D region.

S6 has been detected in the anti-centre direction ($l, b = 176.18$, $b = -2.11$), at a distance estimated to 2 kpc using the extinction signature method by Marshall et al. (2006). The filament-shaped core seen with *Planck* does not coincide with any known object, but is likely associated with the Perseus arm.

S7 has been observed by Ungerechts & Thaddeus (1987) as part of their large CO survey of Perseus, Taurus and Auriga. It is included in their 12th area (see their Table 1), covering 41.8 deg^2, with a distance of 350 pc. For this large region, they estimate a virial mass that is four times higher than the CO mass, showing that this region is out of equilibrium. The *Planck* source is not associated with any known objects in the SIMBAD database.

S8, **S9** and **S10** correspond with *Herschel* SDP sources PCC288, PCC550 and PCC249, respectively. These fields were selected in September 2009 from the cold core detections in the First Light Survey of *Planck*, in order to perform the first follow-up observations of our *Herschel* key-program during the *Herschel* SDP. The fields were mapped with both PACS and SPIRE (with map sizes from 18' to 50'), and the observations have been described in detail in dedicated papers (Juvela et al. 2010, 2011).

Field S8 is located in Cepheus, at the interface between the Cepheus F molecular cloud (Sargent 1977) and the young stellar group Cep OB3b (Jordi et al. 1996), which is one of the youngest nearby stellar groups. It has been suggetsed that this region could show direct evidence for star formation triggered by the OB association. S9 is an active star formation region close the S140 H II region. *Planck* has provided two detections, PCC288-P1 and PCC288-P2 (see Juvela et al. 2010), with the southern source PCC288-P2 being the colder one. The two cores have also been identified in CS $J = 1 \rightarrow 0$ mapping of the area by Tafalla et al. (1993). The field S10 is part of the Musca cloud filament, where *Planck* shows two secure detections of cold cores ($T \sim 11$ K). The cores have been studied previously in ^{13}CO and $C^{18}O$ by Vilas-Boas et al. (1994).

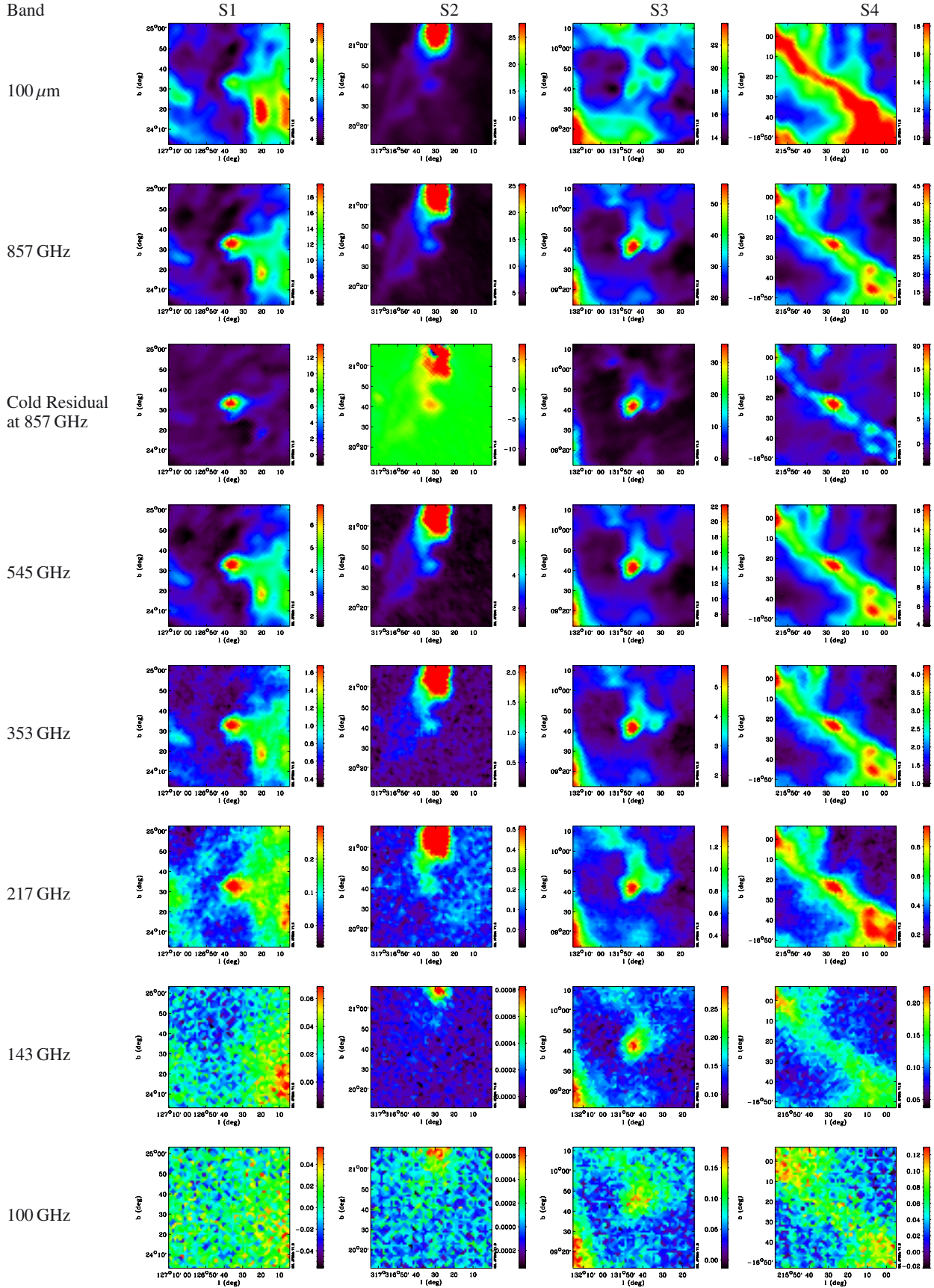**Fig. A.1.** Multi-band emission maps (in MJy/sr) of the sources S1, S2, S3, and S4.

Band	S5	S6	S7	S8

100 μm

857 GHz

Cold Residual
at 857 GHz

545 GHz

353 GHz
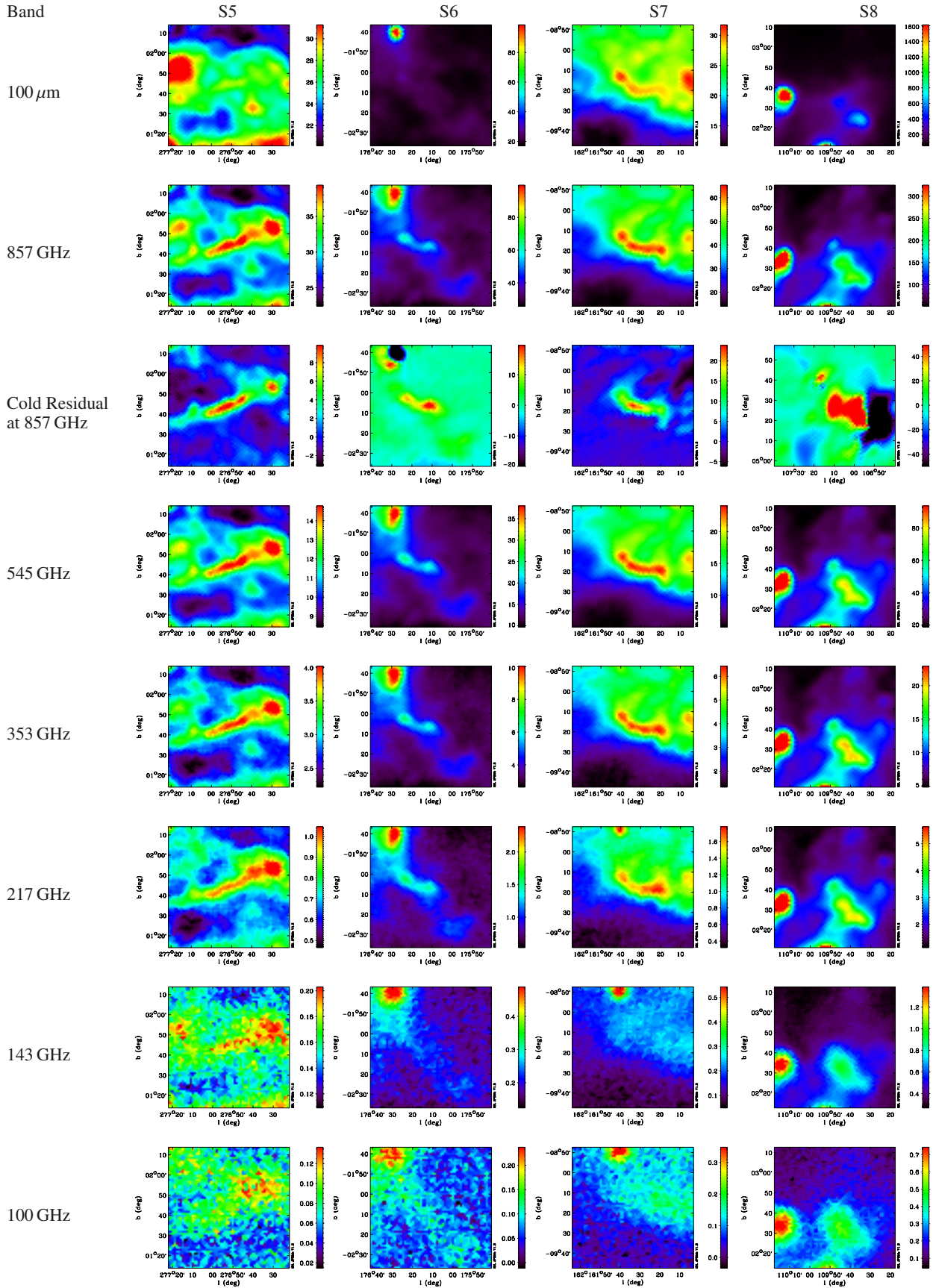
217 GHz

143 GHz

100 GHz

Fig. A.2. Multi-band emission maps (in MJy/sr) of the sources S5, S6, S7, and S8.
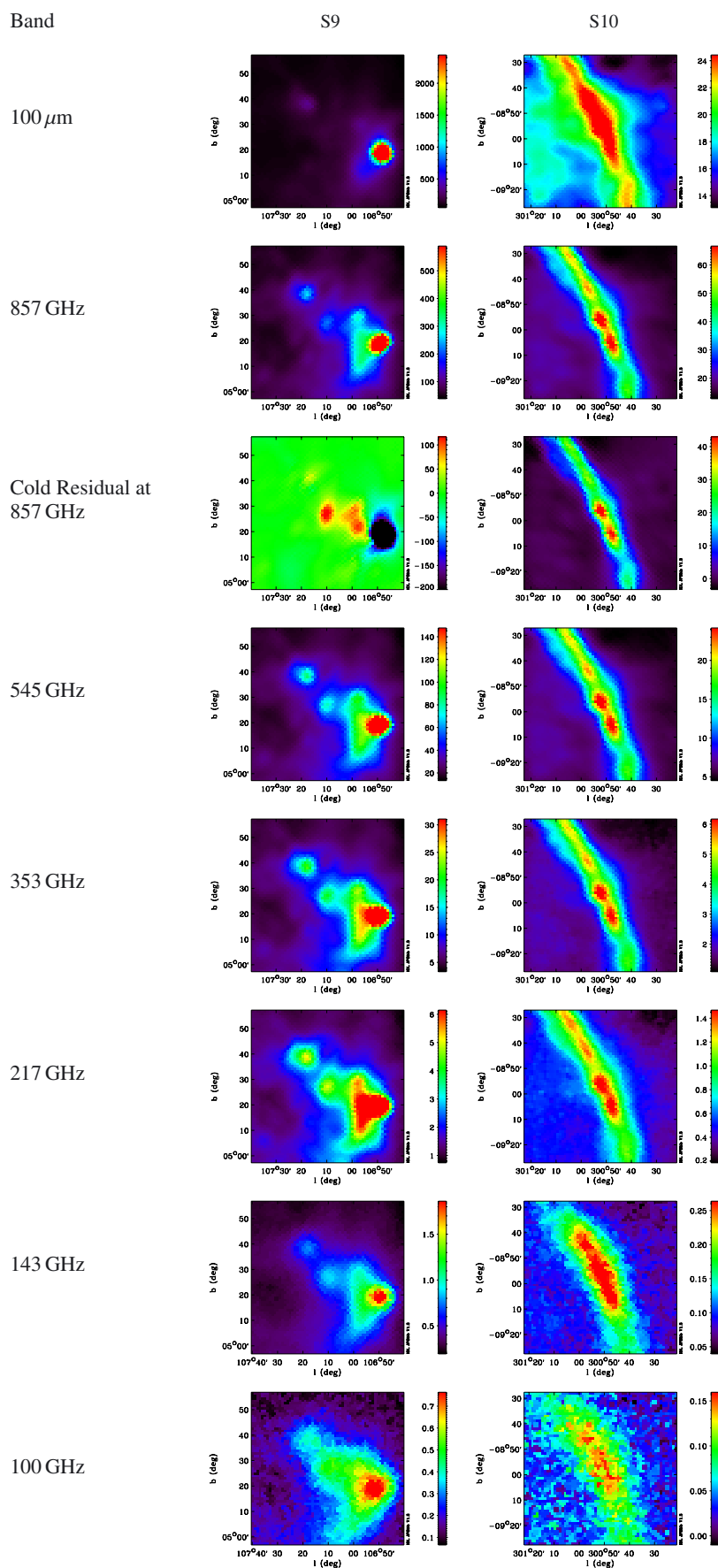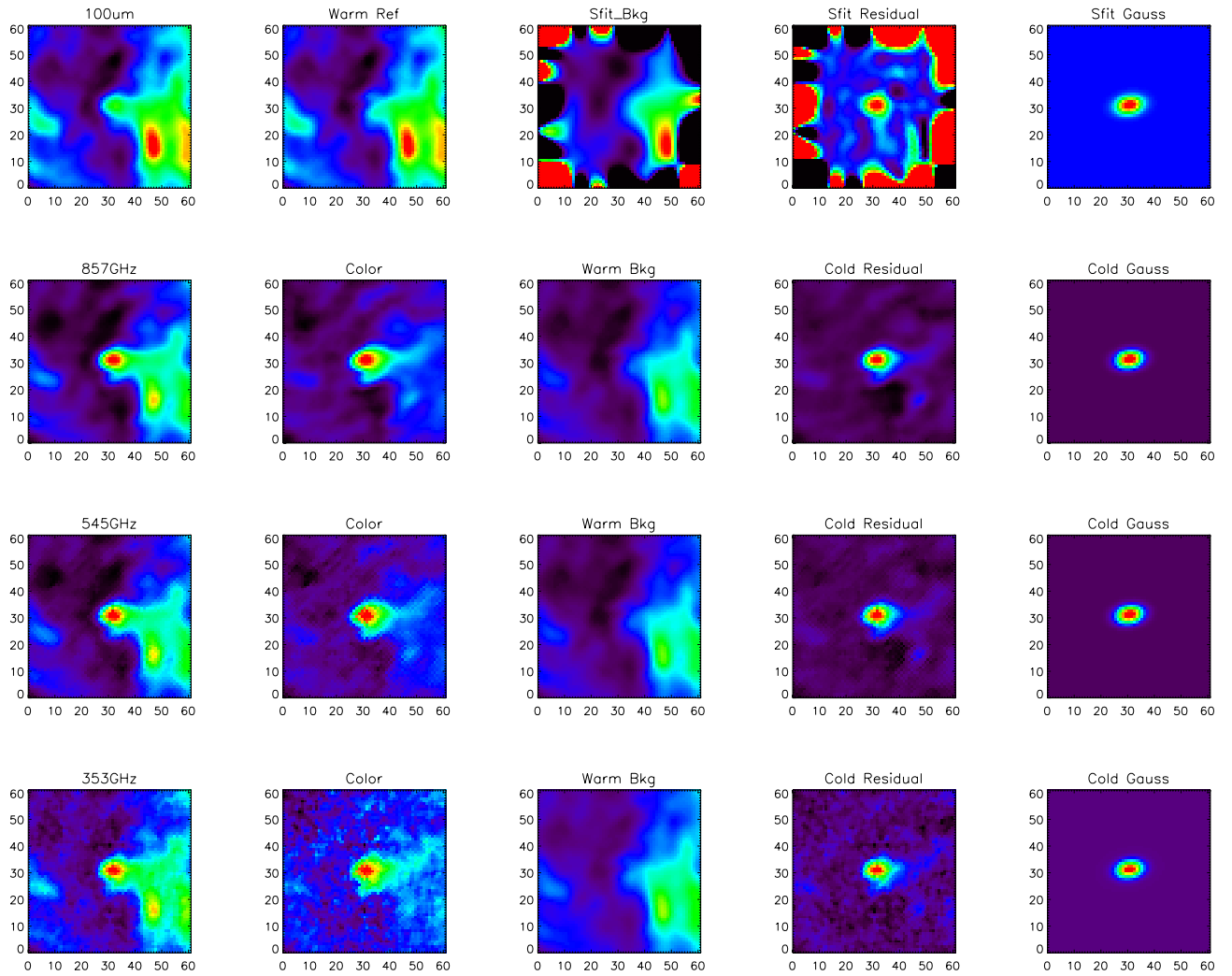
Band	S9	S10

Fig. A.3. Multi-band emission maps (in MJy/sr) of the sources S9 and S10.

Fig. A.4. Illustration of the steps used in the detection and core extraction methods, as applied to source S1. The first column shows the initial surface brightness emission maps in the IRIS and HFI bands. The rows show the process applied to the $100\,\mu$m, 857, 545, and 353 GHz data, respectively. As described in Paper I, the method follows the following main steps: a "Warm Ref" is built from the IRIS $100\,\mu$m map and extrapolated to the *Planck* bands using the local colour estimated around each pixel of the *Planck* map (these colour maps are shown in the second column); the "Warm Bkg" map obtained at a given frequency is then removed from the *Planck* map, revealing the "Cold Residual"; and finally an elliptical Gaussian fit is performed on the colour maps to derive the core size parameters, while aperture photometry is performed on the HFI bands, integrating the signal within the elliptical Gaussian.
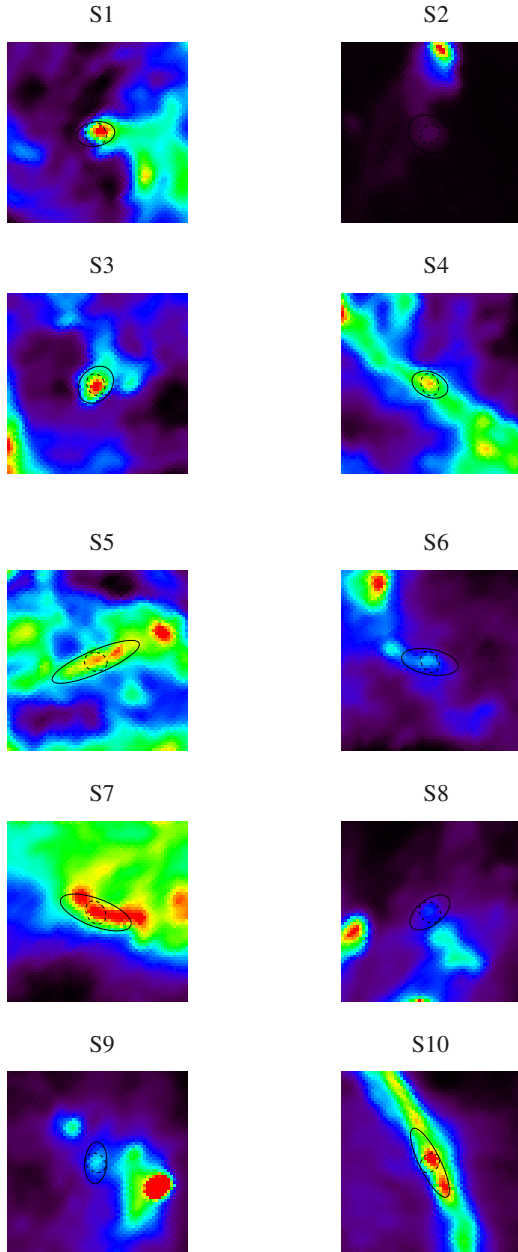
Fig. A.5. Comparison of the source elongation with the beam shape determined with the "FEBeCoP" tool (Mitra et al. 2011). The ellipses correspond to the size of the *Planck* cold clumps derived from the fit; they are plotted at a 2σ level for a better visibility. The dashed circles trace the local beam shape.
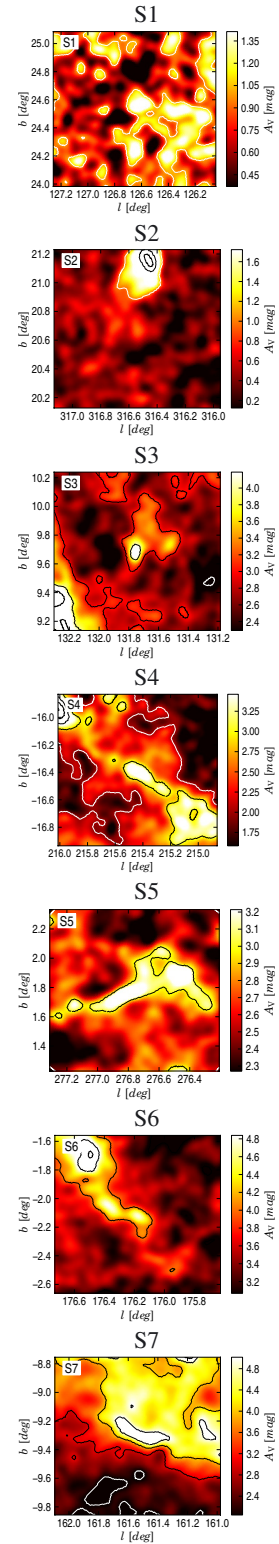
Fig. A.6. Visual extinction maps obtained from 2MASS and the NICER method (cf. Sect. 4.2). The maps are shown at 4.5′ resolution. Contours are drawn at integer values of A_V.

Table A.1. Observational parameters and sensitivity of IRAM observations.

Molecule	Transition	Frequency (MHz)	Beam size (arcsec)	δv (m s^{-1})	rms (K)
1st setting					
^{12}CO	$J = 1 \rightarrow 0$	115271.197	23	200	0.24
^{12}CO	$J = 2 \rightarrow 1$	230537.990	12	100	0.15
2nd setting					
^{13}CO	$J = 1 \rightarrow 0$	110201.370	24	27	0.15
^{13}CO	$J = 2 \rightarrow 1$	220398.686	12	53	0.15
^{13}CO	$J = 1 \rightarrow 0$	110201.370	24	27	0.90[a]
^{13}CO	$J = 2 \rightarrow 1$	220398.686	12	53	0.90[a]
C^{18}O	$J = 1 \rightarrow 0$	109782.182	24	27	0.15
C^{18}O	$J = 1 \rightarrow 0$	109782.182	24	27	0.90[a]
3rd setting					
N$_2$H$^+$	$J = 1 \rightarrow 0$	93173.764[b]	27	31	0.04
C^{18}O	$J = 2 \rightarrow 1$	219560.358	12	53	0.05

Notes. [a] Raw value for on-the-fly mapping. [b] Main hyperfine components, frequency from Pagani et al. (2009).